

Smart optimized structural control of onshore wind turbines with MR dampers

Peter Fakhry^{a,b,*}, Duan Fang^b, Mohammad Osman Tokhi^b, Shady Salem^a

^a Civil Engineering Department, The British University in Egypt, El Sherouk City, Cairo, Egypt

^b School of Engineering, London South Bank University, London, UK

ARTICLE INFO

Keywords:

Wind turbine
Magnetorheological dampers
Particle swarm optimization
Edgewise displacement

ABSTRACT

This paper presents an effective control approach for structural vibration of onshore wind turbines in the edgewise direction. Huge multi mega-watt wind turbines are currently developed to harvest large amounts of energy from the wind. Such designs require the construction of huge slender blades and towers which consequently lead to undesirable structural deformations that hinder the power production and reduce life span of the wind turbine. Many researchers have worked on structural control of wind turbines. However, these efforts neither have resulted in an effective reliable mitigation for deformation of structural elements, nor they have achieved an economical solution in terms of actuators exploitation. The work presented in this paper, however, introduces a particle swarm optimisation-based semi-active controller which exploits magnetorheological dampers to mitigate edgewise blade displacements. Dampers are modelled using neural networks for they are capable of predicting future forces and eliminating control lag. The developed controller is tested at several configurations of actuators placement on a benchmark 5-MW wind turbine. The proposed approach, indeed, showed a significant reduction of over 80% in the peak responses and about 77% of peak-to-peak response of blades against uncontrolled and passive systems which leads to promoting longevity of wind turbines.

1. Introduction

The global concern about climate change has fostered the potential of reducing carbon dioxide emissions. More specifically, the international paradigm shift of producing renewable energy is derived by reducing the energy related carbon emissions which constitute 66% of the total greenhouse gases emissions [1]. In this context, within the past few decades several research works have suggested optimization of production of renewable energy. Distinctively, wind energy is considered as one of the most environment-friendly energy sources. This superiority is due to the fact of being a clean source of energy, compatibility with other land use activities, consuming less water and relatively low gas emissions [1]. The International Energy Agency (IEA) has reported that energy extracted from wind turbines has reached over 1800TWh in 2021 [2]. Moreover, it recorded the highest growth amongst all renewable energy forms. Wind turbine electricity is also expected to reach 7900TWh by the year 2030 that is in collaboration with the plan of zero carbon emissions by the year 2050 [2].

The increasing demand for wind energy over the past few years has motivated the installation of multi megawatt turbines with large di-

mensions of tower and blades [3]. Generating up to 6.3 –MW of power, the cypress 6.0 –164 wind turbine has a blade length of 80m and hub height of 167m [4]. However, such slender and large turbines are susceptible to large dynamic responses and vibrations when subjected to environmental disturbances. Moreover, installation of offshore wind turbines in oceans has gained wide acceptance due to space availability and higher wind intensities [5]. Onshore wind turbines, on the other hand, are subjected to severely high wind intensities if located in highly active wind zones. Such dynamic loading of on/offshore wind turbines leads to undesirable deformations and consequently reduces the lifetime of the structure (wind turbine blades' fatigue) and hinders power production (unsteady energy output).

Structural control provides solution to excessive structural deformation and damage. Noticeable developments have been made in this area over the past decades, especially in control of civil engineering structures [6–9]. Structural control operates in three modes, namely passive, active, and semi-active. Passive control mode is used such that the control force of an actuator cannot be adjusted in response to an external influence and thus it has limited control force capacity. Active control is achieved when the control force is directly actuated through the actuators. On the other hand, semi-active operates by changing

* Corresponding author at: Civil Engineering Department, The British University in Egypt, El Sherouk City, Cairo, Egypt.

E-mail address: peter.fakhry@bue.edu.eg (P. Fakhry).

Nomenclature

α	Angle of attack.	M_{nr}	Non-rotating frame wind turbine mass matrix.
$\alpha_{co,i}$	Rayleigh damping mass proportional factor for the o^{th} element in the i^{th} plane.	M_T	Total tower mass matrix.
a	Axial induction factor.	M_{nac}	Nacelle mass.
a'	Tangential induction factor.	M_o	Overall blade mass.
a_c	Glauert correction factor.	N	Total number of DOFs.
A_{nr}	Non-rotating frame system matrix.	n	Total number of modes for all blade planes.
Ψ_j	j^{th} blade azimuth angle.	Q	Dynamic response controller weighting matrix.
β	Blade pitch angle.	Q_{ext}	Total external loads acting on wind turbine.
$\beta_{co,i}$	Rayleigh damping stiffness proportional factor for the o^{th} structural element in the i^{th} plane.	Ω	Rated rotor speed.
B_{nr}	Non-rotating frame input matrix.	$\omega_{1,i}$	First natural frequency in the i^{th} plane.
C_a	Aerodynamic damping matrix.	$\omega_{2,i}$	Second natural frequency in the i^{th} plane.
C_s	Structural damping matrix.	Q_a	Generalized aerodynamic loads vector.
C_T	Total tower damping matrix.	Q_g	Generalized gravitational loads vector.
C_L	Coefficient of lift.	ϕ	Flow angle.
C_D	Coefficient of drag.	ϕ_i	Mode shape of the i^{th} plane.
C_{nr}	Non-rotating frame wind turbine damping matrix.	\tilde{q}	Generalized coordinates vector.
c	Aerofoil chord length.	$\tilde{q}_{j,i}$	Generalized DOF of j^{th} blade in i^{th} plane.
c_0	Nonlinear velocity roll-off MR damper damping.	$\tilde{q}_{4,h}$	Generalized DOF of tower in i^{th} plane.
c_1	MR damper damping term.	R	Desired controller force weighting matrix.
E	Modulus of elasticity of blades.	ρ_{air}	Air density.
F_D	Vector of MR damper forces.	s	Wind turbulence.
\hat{F}_{i+1}	Next step NN predict MR damper force.	T	Total kinetic energy of wind turbine.
f_c	Blade centrifugal force.	t	Solution time domain.
f_{cd}	MR damper desired control force.	θ	Aerofoil pre-twist angle
$f_{d,j}$	Generalized MR damper force for j^{th} blade.	u	First order filter.
$f_{g,j}$	Generalized gravitational force for j^{th} blade.	T	Total kinetic energy of wind turbine.
G_{nr}	Non-rotating frame controller gain.	t	Solution time domain.
g	Gravitational acceleration.	θ	Aerofoil pre-twist angle
Γ	MR dampers influence all planes matrix.	u	First order filter.
Γ_e	MR dampers influence in-plane matrix.	$u_{j,i}$	Displacement along j^{th} blade in i^{th} plane.
h	Respective tower plane of study.	μ_b	Distributed mass of blade.
I	Blade moment of inertia.	μ_T	Distributed mass of tower.
i	Respective blade plane of study.	V	Total potential energy of wind turbine.
j	Blade under study.	V_{oj}	Total mean wind speed on j^{th} blade.
K_e	Blade elastic stiffness matrix.	\bar{V}_o	Mean wind speed.
K_C	Blade centrifugal stiffness matrix.	ΔV_o	Change in wind speed due to vertical shear.
K_T	Total tower stiffness matrix.	V_{rel}	Aerofoil relative wind speed.
K_g	Blade gravitational stiffness matrix.	V_{l-1}	Previous time step MR damper commanded voltage to NN.
K_{nr}	Non-rotating frame wind turbine stiffness matrix.	V_l	Current time step MR damper commanded voltage to NN.
k_0	MR damper accumulator stiffness.	v	MR damper commanded voltage.
k_1	MR damper stiffness term.	v_j	Total velocity of j^{th} blade.
L	Lagrangian.	v_4	Total velocity of tower.
L_b	Length of blade.	X_l	Current time step MR piston displacement to NN.
L_d	Influence length of MR dampers across the blade.	\dot{X}_l	Current time step MR piston velocity to NN.
L_T	Length of tower.	X_{l-1}	Previous time step MR piston displacement to NN.
l_L	Aerofoil local lift force.	\dot{X}_{l-1}	Previous time step MR piston velocity to NN.
l_D	Aerofoil local drag force.	x	Distance along the blade measured form the root.
l_N	Aerofoil normal or thrust force.	x_d	MR damper piston displacement.
l_T	Aerofoil tangential force.	\dot{x}_d	MR damper piston velocity.
$l_{j,i}$	Generalized aerodynamic loads of j^{th} blade in i^{th} plane.	z	Distance along the tower measured form the ground.
		ξ_o	Damping ratio of o^{th} structural element.
		$\alpha_d, \gamma, n_d, \beta_d, A_d$	MR damper non-linear yielding element parameters.

parameters of the control device (i.e., by altering electric current) and thus adjusting the resisting force for the device used. Semi-active control has the advantage of providing high force capacity of the active control and at the same time using very low power requirement and thus this approach is used in this paper. Any combination between these three modes is referred to as hybrid control mode. Implementation of an

appropriate algorithm will result in improved results and mitigation in the dynamic response of a structure.

Structural control has been recently introduced to mitigate wind turbine structure deformation and dynamic responses whether onshore or offshore [3,8,10–12]. One of the early benchmarks in the field of structural control on wind turbines is that reported in [13], where the

authors have successfully exploited the use of Active Mass Dampers (ATMDs) in wind turbines to control the in-plane blade vibration responses. They have used an Euler Lagrange numerical model for the wind turbine derived from the kinetic and potential energies of the system and have used Tuned Mass Dampers (TMDs) in passive and active modes, where the active mode is realised with linear quadratic regulator (LQR).

Staino and Basu (2013) have developed a numerical model of wind turbine system using the Lagrangian-Euler approach considering the time variant structural properties and accounting for the variable rotor speed caused by system faults [14,15]. They have proposed the application of an active tendon system mounted onto a truss/frame structure placed inside each blade. They implemented a LQR to determine the optimal active control forces generated in the tendons to control the large edgewise displacements induced in the blades due to variations in rotor speed. Their simulation results show a noticeable decrease in the tip displacements for onshore wind turbines. Zhang *et al.* (2016) have used a Tuned Liquid passive Damper (TLD) to control the side-to-side vibration of onshore wind turbines [16]. They were motivated by the negative effect that arises as a result of the combination of the lateral tower vibration with the drivetrain torsional moments, where the latter results in instability in the generator torque and thus fluctuations in the produced power. As TLDs are highly non-linear devices and their control force is affected by many parameters, the authors have chosen to apply Real-Time Hybrid Testing (RTHT) algorithm as a modelling technique for their system. Sarkar and Chakraborty (2018) have also developed a semi-active control algorithm for controlling the vibration response of an onshore wind turbine tower using MR-TLCD [17] and have tested the controller with various wind speeds. Caterino (2015) tested a semi-active control scheme with MR dampers for reducing the dynamic structural responses of onshore wind turbines in terms of tower base bending stresses and top displacement experimentally on a 1/20 scaled wind turbine model [18]. The semi-active control strategy was achieved by placing MR dampers at the tower base. Caterino (2015) defined the concept of a variable restraint to resist the tower loads such that it is made of a cylindrical hinge, two springs and two MR dampers. The test results have shown a reduction in bending stresses demand of 64% in some cases but at the cost of increasing the top displacement by 29%.

Moreover, Chen *et al.* (2015) have used MR dampers inside wind turbine blades for vibration reduction [19]. They have implemented a fuzzy logic Memdani model with the stroke of the damper piston and its velocity as inputs and have deduced that as the number of controllers is increased and placed closer to the tip, suppression of dynamic disturbances is more effective. Recent explorations have revealed efforts in structural control of wind turbines; however, the achieved results need to be more reliable in terms of dynamic disturbance suppression and at the same time using minimum power consumption.

Particle Swarm Optimization (PSO) is integrated with control systems for their good adaptation of different controllers and accuracy. Kumar and Jerome (2014) used PSO to control an inverted pendulum underactuated system. They reported the use of PSO for search of LQR weighting matrix R in which good control results were achieved [8]. Moreover, Kumar *et al.* (2018) applied an adaptive PSO to enhance controller performance in time-domain of near resonance for civil structures when subjected to strong earthquakes using MR dampers [20]. It is needless as well to stress on the importance of Neural Networks (NNs) and their use in structural control systems. Wang and Liao (2005) developed two different types of NN for modelling and control of MR dampers by generating command voltage in a semi-active control mode [21].

In this paper, a novel optimized controller using particle PSO semi-active control is proposed for control of excessive displacements of wind turbine blades in the edgewise directions. Semi-active control is achieved using MR dampers placed inside each blade considering different locations and/or numbers. Numerical models of actuators are developed using NNs for their robustness and high predictive accuracy

in predicting non-linear systems behaviour. Several scenarios of implementing MR dampers with various configurations and controllers are investigated and tested, which demonstrate the efficacy of the proposed approach. Fig. 1 shows a scheme for the proposed control process.

2. Wind turbine and external loads models

In this section a multi-modal numerical model of a horizontal axis wind turbine is developed based on the Euler-Lagrangian energy formulation. Dynamic equation of motion is derived for a three-bladed horizontal axis wind turbine with a tower fixed to the ground such that dynamic coupling between the blades and tower is achieved. As shown in Fig. 2, the three blades are modelled as Euler-Bernoulli elastic beams with distributed mass $\mu_b(x)$, overall mass M_o and elastic stiffness $EI(x)$ along its length. Blades are considered as cantilever beams fixed at the hub and the rotor fixed with the tower. The tower is considered as a generalized single degree of freedom (DOF) system with due consideration the tower modal mass M_T (as depicted in Fig. 2) and masses of the nacelle and hub as M_{nac} . The developed model is capable of solving for dynamic responses of blades in the edgewise and flapwise directions. Similarly, the tower responses can be expressed in the side-to-side and fore-aft senses. Moreover, the model can capture the coupled responses between in-plane and out-of-plane that occur due to the pre-twisted blades.

The tower stiffness and damping terms in the developed numerical model in the side-to-side and fore-aft modes are denoted as K_T and C_T , respectively where C_T is the summation of the structural and aerodynamic damping. The developed model accounts for variation in rotor speed. The rotor is set to rotate at the rated speed Ω (rad/sec) and the azimuth angle $\Psi_j(t)$ (rad) of blade j is expressed in terms of time t as

$$\Psi_j(t) = \Omega t + \frac{2\pi}{3}(j-1), j = 1, 2, 3 \quad (1)$$

Structural elements with distributed mass and elasticity are often modelled as generalized single or multi DOF systems, where their dynamic response is expressed as a function of a generalized or a benchmark coordinate [22]. In this work, the generalized coordinate is chosen to be the tip displacements of the blades in the edgewise and flapwise directions as well as the tower-top/nacelle motion in the side-to-side and fore-aft directions. Moreover, for simplicity, only the fundamental blade modes in the edgewise and flapwise directions are considered. Likewise, the first mode for side-to-side and fore-aft deflections are considered for the tower. The total number of DOF for the horizontal axis wind turbine numerical model is $N = 3n + 2 = 8$, where n is the total number of mode shapes considered for one blade. The generalized coordinates can be expressed as

$$\tilde{q}(t) = \left\{ \tilde{q}_{1,in}(t) \tilde{q}_{1,out}(t) \tilde{q}_{2,in}(t) \tilde{q}_{2,i}(t) \dots \tilde{q}_{j,i}(t) \tilde{q}_{4,h}(t) \right\}_{\in \mathbb{R}^{N \times 1}}^T \quad (2)$$

where N is the total number of DOF for the horizontal axis wind turbine, i represents the plane of interest for the blade (*in* or *out*) and h represents the plane of interest for the tower (*ss* or *fa*). As shown in Fig. 2, blade displacement at any given x position from the blade root is expressed as modal superposition of the generalized DOF for the blade as formulated as

$$u_{j,i}(x, t) = \phi_i(x) \tilde{q}_{j,i}(t) \quad (3)$$

The Euler-Lagrange equation for forced vibration dynamic systems is expressed in terms of partial derivatives of the Lagrangian L with respect to the generalized coordinate and its time derivative as

$$\frac{d}{dt} \left(\frac{\partial L}{\partial \dot{\tilde{q}}} \right) = \left(\frac{\partial L}{\partial \tilde{q}} \right) + Q_{ext} + \Gamma F_D \quad (4)$$

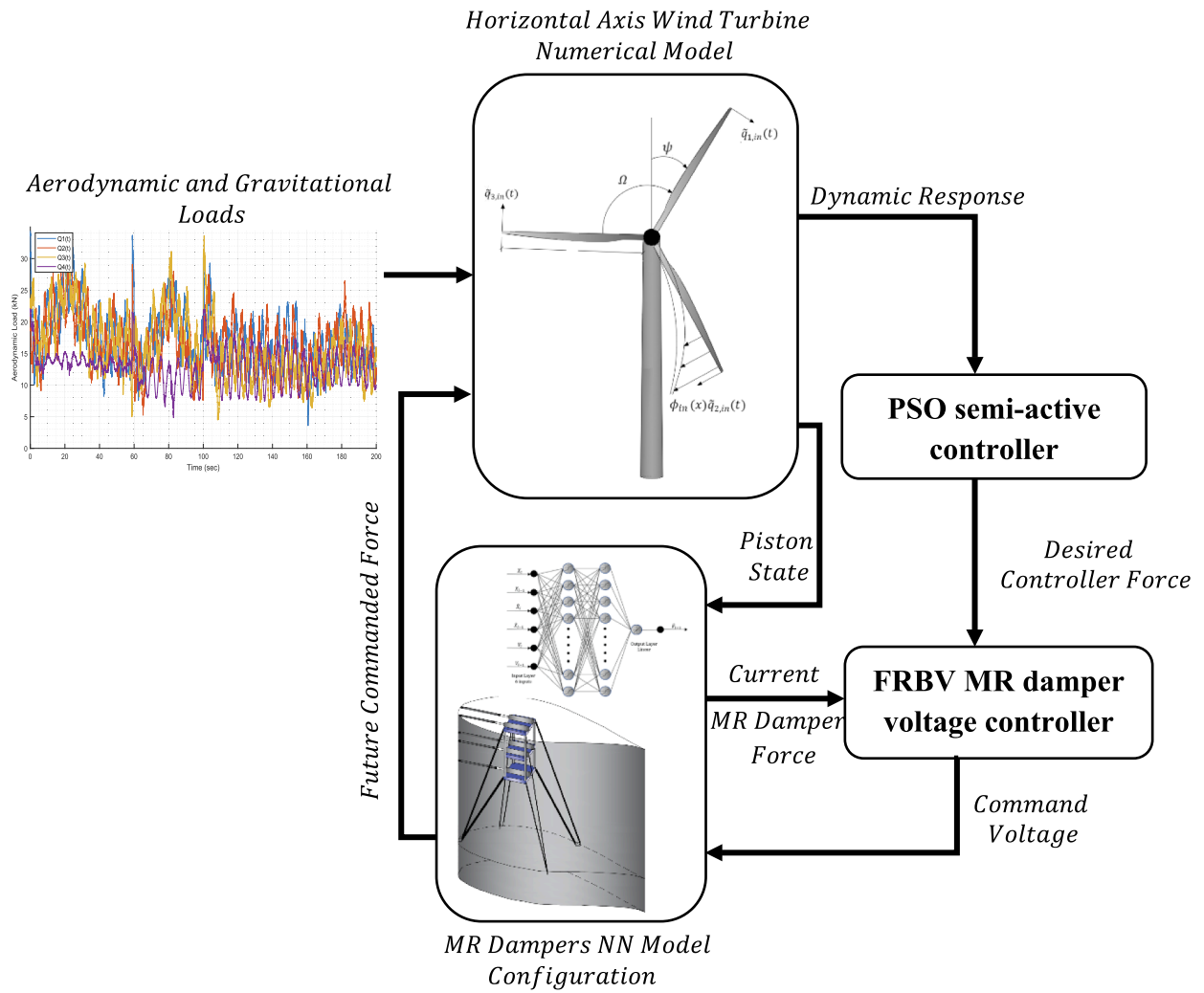


Fig. 1. Proposed semi-active control scheme.

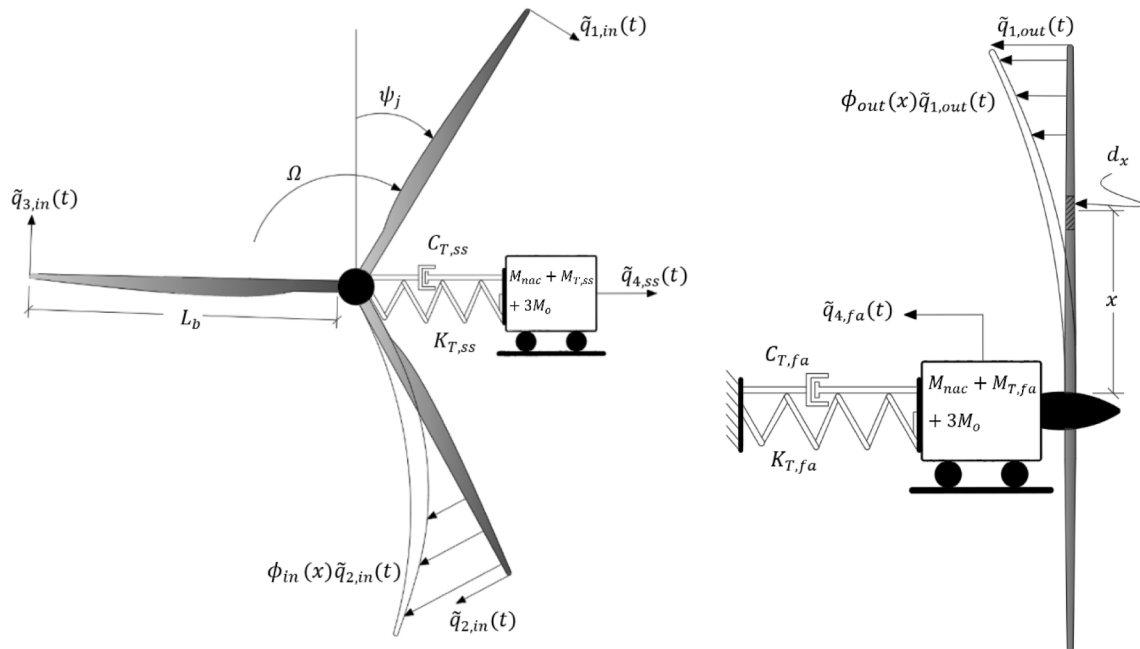


Fig. 2. Numerical model and generalized DOF definition for wind turbine.

where Q_{ext} represents the aerodynamic and gravitational loads acting on the wind turbine blades and tower, respectively and $\in R^{N \times 1}$ while F_D is a vector of MR damper forces and Γ is influence matrix indicating positions of actuators. The Lagrangian L is the difference in kinetic T and potential V energies of the system as

$$L = T - V \quad (5)$$

2.1. Wind turbine model

2.1.1. Kinetic energy

The total kinetic energy of the system arises from the velocity of the three blades in the edgewise and flapwise directions as well as the velocity of the tower in the side-to-side and fore-aft directions. As such, the total kinetic energy of the system can be formulated as

$$T = \frac{1}{2} \left[\sum_{j=1}^3 \left[\int_0^{L_b} \mu_b(x) v_j(x, t)^2 dx \right] + \left[\int_0^{L_T} \mu_T(z) v_T(z, t)^2 dz \right] + (M_{hub} + M_{nac}) v_T(L_T, t)^2 \right] \quad (6)$$

where v_j is the total velocity in edgewise and flapwise directions of an incremental part along the blade j located at distance x from the hub at time t . Similarly, v_T is the total velocity in the side-to-side and fore-aft directions of an incremental segment along the tower located at distance z from the ground at time t .

The velocity of the blade is affected mainly by its rotation, its deflection and the effect of the tower and nacelle motion on it as illustrated in Fig. 3. Thus,

$$v_j(x, t) = \Omega x - \Omega (\phi_{in}(x) \tilde{q}_{j,in}(t)) + \sum_{i=in}^{out} \phi_i(x) \cdot \tilde{q}_{j,i}(t) + \cdot \tilde{q}_{4,ss}(t) \cos(\psi_j(t)) + \cdot \tilde{q}_{4,ss}(t) \sin(\psi_j(t)) + \cdot \tilde{q}_{4,fa}(t) \quad (7)$$

$$v_T(z, t) = \sum_{i=ss}^{fa} \phi_i(z) \cdot \tilde{q}_{4,i}(t)$$

2.1.2. Potential energy

Potential energy of the system arises from elastic stiffness of the blades in bending K_e , geometrical or centrifugal stiffening K_C of the blades that arises from tensile forces induced due to rotation, gravitational stiffening K_g arising from gravity forces acting on the blades due to rotation of the rotor and tower/nacelle potential energy. Finally, the bending stiffness associated with the tower K_T . The total potential en-

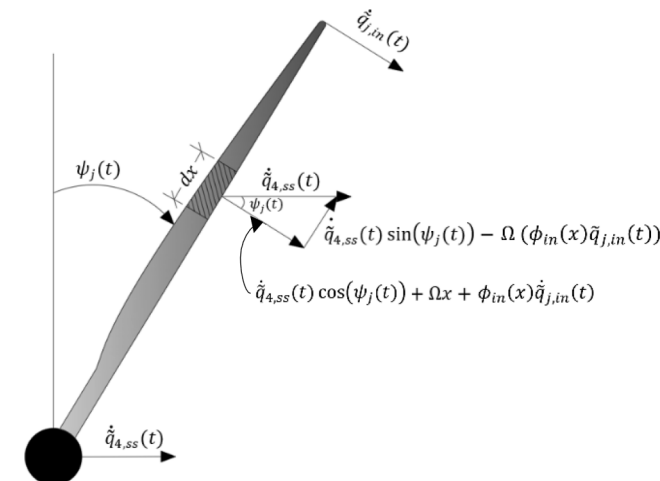


Fig. 3. Velocity components acting on a wind turbine blade incremental length.

ergy for the horizontal axis wind turbine system is thus given as

$$V = \frac{1}{2} \sum_{j=1}^3 \left[\left(\sum_{i=in}^{out} (K_{e,ii} + K_{c,i} + K_{g,j,i} (\tilde{q}_{j,i}(t))^2) + K_{e,inout} \tilde{q}_{j,in}(t) \tilde{q}_{j,out}(t) \right) + \frac{1}{2} \sum_{h=ss}^{fa} K_{T,h} (\tilde{q}_{4,h}(t))^2 \right] \quad (8)$$

The tensile forces acting on the blade due to the effect of centrifugal and gravitational stiffening are given as [23]

$$f_c(x) = \Omega^2 \int_x^{L_b} \mu_b(\rho) \rho d\sigma \quad (9)$$

$$f_{g,j}(x) = -g \cos(\psi_j(t)) \int_x^{L_b} \mu_b(\rho) \rho d\sigma \quad (10)$$

where ρ is the distance from the point x along the blade. Using equations (9) and (10) the stiffness terms can be obtained as

$$K_{c,i}(x) = \int_0^{L_b} f_c(\phi_i(x'))^2 dx = \Omega^2 \int_0^{L_b} \left[\int_x^{L_b} \mu_b(\rho) \rho d\sigma \right] (\phi_i(x'))^2 dx \quad (11)$$

$$K_{g,j,i}(x) = -g \cos(\psi_j(t)) \int_0^{L_b} f_{g,j}(x) (\phi_i(x'))^2 dx = -g \cos(\psi_j(t)) \int_0^{L_b} \left[\int_x^{L_b} \mu_b(\rho) \rho d\sigma \right] (\phi_i(x'))^2 dx \quad (12)$$

and $K_{e,ii}$ is

$$K_{e,ii}(x) = \int_0^{L_b} EI_{ii}(x) (\phi_i(x'))^2 dx \quad (13)$$

where, $\phi_i(x)'$ and $\phi_i(x)''$ are the first and second order derivatives with respect to x , respectively. The elastic stiffness can also be found through the relation between the mass and the square of the spectral matrix. By substituting Eqs. (11), (12) and (13) into Eq. (8) the potential energy of the wind turbine can be obtained.

2.2. BEM and generalized external loads

2.2.1. Blade element momentum theory

In this work, aerodynamic loads acting on the blades and tower are modelled using the Blade Element Momentum (BEM) theory. The mentioned algorithm combines the standard momentum theory and strip or element theory to model wind loads acting on wind turbines instead of employing the tedious and difficult CFD algorithms [29]. Moreover, BEM is based on some parameters such as, but not limited to, the rotor speed Ω , mean wind speed V_o , turbulence intensity s and geometrical aerofoil sections.

To account for the variation of wind loads with the wind turbine's height, vertical wind shear effect is added to the mean wind velocity as a cosine wave of amplitude dependant on the azimuthal angle expressed as

$$V_{o,j}(x, t) = \bar{V}_o + \frac{x}{L_b} \cos(\Psi_j(t)) \Delta V_o \quad (14)$$

As shown in Fig. 4, each blade is discretized into a number of elements each located at a distance x from the root, with a chord of $c(x)$ and a width of dx . Assuming no aerodynamic interaction between blade elements, the axial and induction factors a and a' can be found and hence the tangential (forces acting in the edgewise direction) and normal (forces acting in the flapwise direction) force components can be found accordingly. Once all blade elements forces are computed, the generalized total blade force through the corresponding generalized DOF can be computed using numerical integration along the blade's span (Eq. (20)). Since blades are rotating, they experience the coming wind speed.

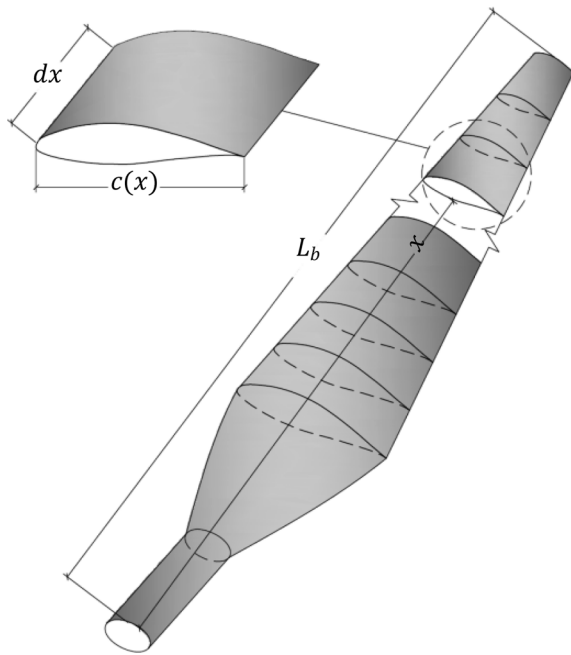


Fig. 4. Blade modelling using BEM.

According to Fig. 5, one can deduce V_{rel} as

$$V_{rel}(x, t) = \sqrt{\Omega^2 x^2 (1 + a')^2 + (V_o(1 - a) + s(t))^2} \quad (15)$$

where $V_{rel}(x, t)$ is the relative velocity that an aerofoil section at a distance x along the blade's length and time t experiences between its rotating speed and s the turbulent wind speed. In addition, the wind flow angle ϕ and angle of attack α on the blade are given by

$$\phi(x, t) = \tan^{-1} \left(\frac{V_o(1 - a) + s(t)}{\Omega x(1 + a')} \right) \quad (16)$$

$$\alpha(x, t) = \phi(x, t) - \beta(t) - \theta(x)$$

The local lift and drag forces for the blade element can be expressed as [29]

$$l_L(x, t) = \frac{1}{2} \rho_{air} V_{rel}^2(x, t) c(x) C_L(\alpha) \quad (17)$$

$$l_D(x, t) = \frac{1}{2} \rho_{air} V_{rel}^2(x, t) c(x) C_D(\alpha)$$

where C_L and C_D are the lift and drag coefficients, respectively for a specific aerofoil section and are dependent on the local angle of attack. As elaborated in Fig. 5, l_N and l_T are defined as the normal or thrust and tangential force given as where correspondingly

$$l_T(x, t) = l_L(x, t) \sin(\varnothing) - l_D(x, t) \cos(\varnothing) \quad (18)$$

$$l_N(x, t) = l_L(x, t) \cos(\varnothing) + l_D(x, t) \sin(\varnothing)$$

which, match the flapwise and edgewise forces. It is worth mentioning that l_T is the force that finally drives the blades to rotate. Two modifications on the calculation of axial induction factor a have been introduced to the BEM algorithm. The first one is Prandtl's tip loss factor which is added to correct the concept of infinite number of blades assumed by the momentum theory whilst the second factor is Glauert method which accounts for higher values of a than a specified value a_c . More details on solving for aerodynamic loads using BEM can be found in [29].

2.2.2. Generalized external loads

External generalized applied loads Q_{ext} in Eq. (4) is expressed in terms of combined aerodynamic and gravitational loads such that

$$Q_{ext} = Q_a + Q_g \quad (19)$$

where, Q_a is the applied wind load on the blades and nacelle in the in-plane and out-of-plane directions and Q_g is the gravitational load due to the weight of the blades. It is to be noted that Q_g , as a load, is different from the stiffening effect due to gravity in section 2.1.2. Aerodynamic and gravitational loads are applied as modal loads acting along the generalized corresponding DOF which is eventually the blade tip as

$$Q_{a,j,i}(t) = \int_0^{L_b} \phi_i(x) l_{j,i}(x, t) dx \quad (20)$$

where $l_{j,i}$ is the respective aerodynamic load on blade j in the edgewise (tangential) or the flapwise (normal) directions calculated using the blade element momentum (BEM) theory algorithm while the loads that

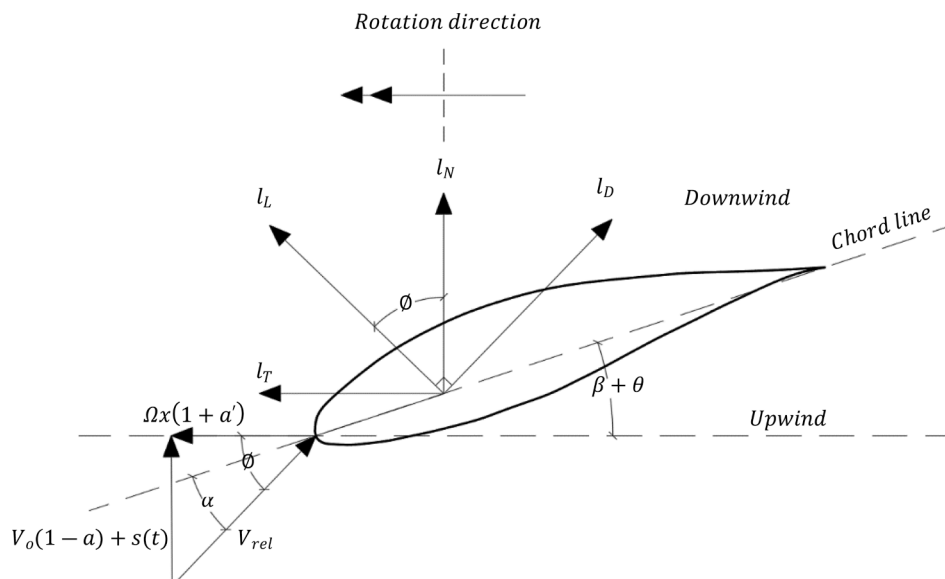


Fig. 5. Velocity Triangle and Forces acting on a Typical Aerofoil using BEM.

act on the nacelle are given by

$$Q_{a,4,ss}(t) = \sum_{j=1}^3 \int_0^{L_b} l_{j,in}(x,t) \cos(\psi_j(t)) dx \quad (21)$$

$$Q_{a,4,fa}(t) = \sum_{j=1}^3 \int_0^{L_b} l_{j,out}(x,t) dx \quad (22)$$

where $Q_{a,4,ss}(t)$ and $Q_{a,4,fa}(t)$ are the nacelle/tower top aerodynamic loads acting in the side-to-side and fore-aft directions, respectively. The MR damper forces are applied on blades as modal loads such that

$$F_D = \left\{ \begin{array}{l} f_{d,1,i} \\ f_{d,2,i} \\ f_{d,3,i} \end{array} \right\}_{\in \mathbb{R}^{3 \times 1}} \quad (23)$$

$$f_{d,j} = \int_{L_b-L_d}^{L_b} \phi_i(x) dx \widehat{F}_{j,i}(t) \quad (24)$$

where, $\widehat{F}_{j,i}$ is the commanded force of the MR damper in direction i as installed in blade j predicted from NN and L_d is the distance covering the dampers position as shown in Fig. 8. The gravitational load is given by

$$Q_{g,j}(t) = g \int_0^{L_b} \mu_b(x) \phi_m(x) dx \sin(\psi_j(t)) \quad (25)$$

where $Q_{g,j}$ is the generalized gravity load acting on the blade j . It is worth mentioning that no gravity loads act on the nacelle in any direction as it is transmitted to the ground via the tower as well as no gravity loads act in the blade's out-of-plane direction.

2.3. Dynamic equation of motion and state space model

As the wind turbine's kinetic (T) and potential (V) energies have been evaluated in Eq. (6) and Eq. (8), respectively, the Lagrangian in Eq. (5) can now be evaluated. Moreover, by partial differentiation of the Lagrangian the Euler-Lagrange equation in Eq. (4) is obtained. Rearranging terms, the dynamic equation of motion can be written as

$$\mathbf{M}(t)\ddot{\mathbf{q}}(t) + \mathbf{C}(t)\dot{\mathbf{q}}(t) + \mathbf{K}(t)\mathbf{q}(t) = \mathbf{Q}_{ext}(t) + \mathbf{\Gamma}F_D(t) \quad (26)$$

Indeed, all system matrices are 8×8 which accounts for only two DOF for each blade and two for the tower. The proposed numerical model has the advantage and novelty of considering the interaction between the in-plane and out-of-plane mode which is dictated by the blade's pre-twist and will be sacrificed if the wind turbine is only modelled with one DOF for the blade and one for the tower. The developed system is thus a time variant system with $2N$ states and a state equation as

$$\dot{\mathbf{x}}(t) = \mathbf{A}(t)\mathbf{x}(t) + \mathbf{B}(t)\mathbf{Q}_{ext}(t) + \mathbf{E}(t)F_D(t) \quad (27)$$

Such that

$$\mathbf{A}(t) = \begin{bmatrix} \mathbf{0}_{8 \times 8} & \mathbf{I}_{8 \times 8} \\ -\mathbf{M}(t)^{-1}\mathbf{K}(t) & -\mathbf{M}(t)^{-1}\mathbf{C}(t) \end{bmatrix}_{\in \mathbb{R}^{16 \times 16}}, \mathbf{B}(t) = \begin{bmatrix} \mathbf{0}_{8 \times 8} \\ -\mathbf{M}(t)^{-1} \end{bmatrix}_{\in \mathbb{R}^{16 \times 8}} \quad (28)$$

$$\mathbf{E}(t) = \begin{bmatrix} \mathbf{0}_{8 \times 3} \\ -\mathbf{M}(t)^{-1}\mathbf{\Gamma} \end{bmatrix}_{\in \mathbb{R}^{16 \times 3}}, \mathbf{\Gamma} = \begin{bmatrix} 1 & 0 & 0 \\ 0 & 0 & 0 \\ 0 & 1 & 0 \\ 0 & 0 & 0 \\ 0 & 0 & 1 \\ 0 & 0 & 0 \\ 0 & 0 & 0 \\ 0 & 0 & 0 \end{bmatrix}_{\in \mathbb{R}^{8 \times 3}}, \text{ for edgewise control} \quad (29)$$

The overall stiffness matrix of the blade accounts for the elastic, gravitational and centrifugal effects, and blade damping as given in

details in Appendix A. The overall damping of the blade and tower is the linear summation of structural and aerodynamic damping such that

$$\mathbf{C}(t) = \mathbf{C}_s(t) + \mathbf{C}_a + \overline{\mathbf{C}}(t) \quad (30)$$

where $\mathbf{C}_s(t)$, \mathbf{C}_a and $\overline{\mathbf{C}}(t)$ are the structural, aerodynamic and effect of rotor speed damping matrices, respectively. According to [17,24,25] aerodynamic damping for blades is given as

$$C_{ba,i} = \frac{1}{2} \rho_{air} \Omega \frac{dC_l}{d\alpha} \int_0^{L_b} xc(x) \phi_i(x)^2 dx \quad (31)$$

where $c(x)$ is the chord length at distance x along the blade's length. The rate of change of lift coefficient with angle of attack, $\frac{dC_l}{d\alpha}$, is constant and equal to 2π before the blade goes into stall. It is worth mentioning that aerodynamic damping in the edgewise direction is very low (close to zero) compared to the flapwise direction. As for the tower, aerodynamic damping is the sum of those of the three blades given as

$$C_{Ta,i,k} = \sum_{j=1}^3 C_{ba,j,h} \quad (32)$$

Moreover, in this paper Rayleigh's classical damping method is adopted to formulate structural damping for the blades and tower [22,26]. Mass and stiffness proportional factors for structural damping were derived, respectively according to [27] as

$$\alpha_{co,i} = \frac{2\omega_{1,i}\omega_{2,i}\xi_o(\omega_{1,i} - \omega_{2,i})}{(\omega_{1,i}^2 - \omega_{2,i}^2)}, \beta_{co,i} = \frac{2\xi_o(\omega_{1,i} - \omega_{2,i})}{(\omega_{1,i}^2 - \omega_{2,i}^2)} \quad (33)$$

Such that o is the structural element considered (blade or tower) where ξ_b and ξ_T are the damping ratios taken for all modes equal to 0.47% for blade and 1% for tower, respectively [28]. All equations regarding system matrices are explained in Appendix A. It is deduced from Eq. (28) and Eq. (29) that the developed system is not a reduced order system and simulations take place such that all DOFs are active. However, another reduced order system is used for obtaining the controller gain as discussed in section 4.

3. MR damper modelling techniques and configuration

3.1. Modified Bouc-Wen model

MR dampers as structural control devices have gained much attention over the past decades. These semi-active control devices had been used extensively in the structural control area on high-rise buildings and for mitigation of dynamic responses in bridges and wind turbines [30–35]. Moreover, MR dampers have been integrated in the structural control of wind turbines to mitigate dynamic responses of different structural elements [18,19,36,37]. Among the advantages of MR dampers are that they can be formulated into a high range of force output. In this paper, and according to the induced wind loads on the wind turbine's blades, a 5000N maximum force damper is utilized. According to literature, many types of mechanical models can be formulated to predict the force produced by MR dampers with specific voltage or current as input. A prevalent numerical model that can predict the MR damper force is the one developed by [38]. It is a modification of the well-established Bouc-Wen mechanical model (also known as the Spencer model). However, the modified version is more accurate since it accounts for the effects of low velocities and the accumulator stiffness present in the damper. This model has been applied extensively in structural control works employing MR dampers. Fig. 6 shows a schematic representation of the modified Bouc-Wen mechanical model, where the force F is the linear combination of the spring stiffness k_1 force and the dashpot c_1 force as

$$F = c_1\dot{y} + k_1(x_d - x_o) \quad (34)$$

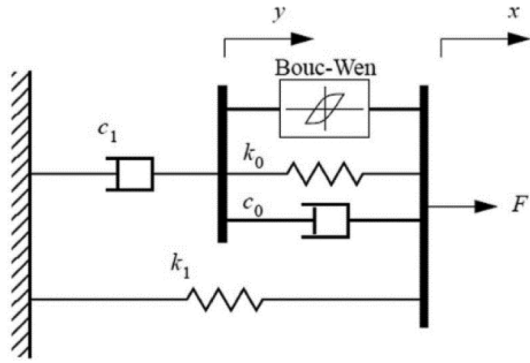


Fig. 6. Modified Bouc-Wen mechanical model.

where \dot{y} , velocity of the dashpot c_1 is governed by the Bouc-Wen hysteresis loop as

$$\dot{y} = \frac{1}{(c_0 + c_1)} \left[\alpha_d z + c_0 \dot{x}_d + k_0 (x_d - y) \right] \quad (35)$$

and the evolutionary variable z is governed by

$$\dot{z} = -\gamma \left| \dot{x}_d - \dot{y} \right| z \left| z \right|^{n-1} - \beta_d \left(\dot{x}_d - \dot{y} \right) \left| z \right|^{n_d} + A_d \left(\dot{x}_d - \dot{y} \right) \quad (36)$$

where x_d is the displacement of the damper piston, y is the displacement of the dashpot c_1 as interpreted in Fig. 6. $\gamma, n_d, \beta_d, A_d$ are the parameters regarding the Bouc-Wen hysteresis loop where they can control the non-linear behaviour of the yielding element [39]. The modified Bouc-Wen model also accounts for the change of the hysteresis non-linear loop in response to the applied voltage where yield stresses and viscous damping terms have been modified as

$$\alpha_d(u) = \alpha_a + \alpha_b u \quad (37)$$

$$c_0(u) = c_{0a} + c_{0b} u$$

$$c_1(u) = c_{1a} + c_{1b} u$$

where u is the output of a first order filter that accounts for the dynamics introduced to the system for the MR fluid to reach rheological equilibrium [38] and is governed by

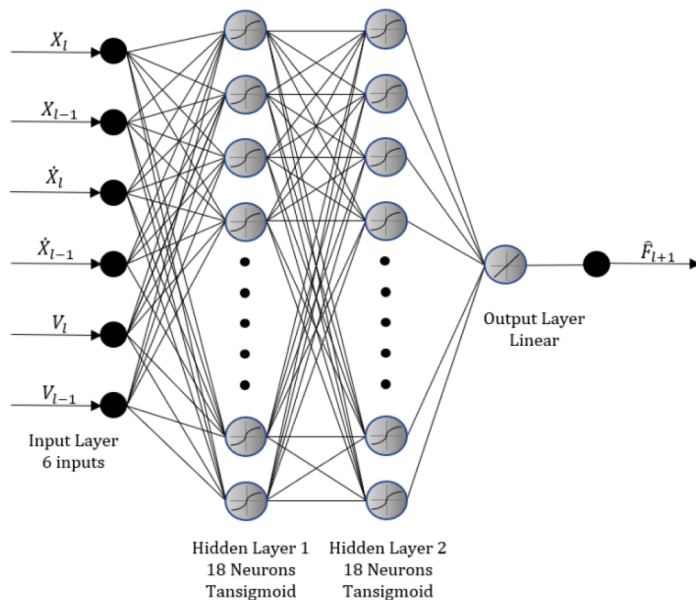


Fig. 7. MR damper FNN model.

$$\dot{u} = -\eta(u - v) \quad (38)$$

where v is the voltage applied to the current driver to the damper and $1/\eta$ is the time constant of this first order filter. A constrained optimization algorithm was implemented to obtain the 14 parameters controlling the MR damper force response through Eqs. (34)–(38) [38,39]. It worth mentioning that the current study introduced the voltage-based MR dampers controller, however, the same methodology is still valid when applying different controlling states (such as current driver).

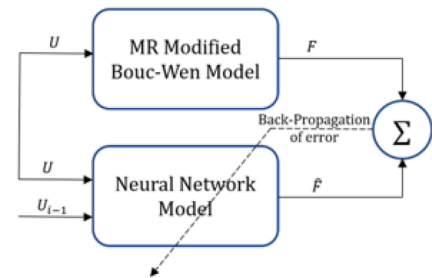
3.2. MR damper Neural network model

To further increase the robustness of an MR damper mechanical model, NNs may be used. In the works by [21,40–42] NNs have been utilized, either as direct model or model accounting for inverse dynamics, to predict the actuated force or the input voltage to the current driver, if used as a voltage controller. In this paper a Feedforward Neural Network (FNN) is developed to overcome the MR damper non linearities and tedious solution of differential equations. The proposed network comprises of two hidden layers each with 18 neurons each with a tansigmoid transfer function for the MR damper identification and an output layer employing linear transfer function.

As depicted in Fig. 7, the proposed FNN is designed with inputs X_l, \dot{X}_l and V_l representing the piston displacement, velocity, and input voltage, respectively such that l is the respective time instant of prediction. Moreover, inputs at the previous time step such as piston displacement, velocity, and input voltage, denoted by X_{l-1}, \dot{X}_{l-1} and V_{l-1} respectively, are also fed as input to the FNN. It is worth mentioning that the MR damper force is not decided to be used as an input to the FNN to eliminate the need for further placing force transducers in the blade's aerofoil vicinity. Training data found in [21] was used in training the proposed FNN as shown in Fig. 7 where back-propagation of error was employed to adjust the weights of the network. This FNN outputs a predicted future MR damper force \hat{F}_{l+1} and thus synchronizes with the estimated controller force. It is worth noting that the developed FNN saved significant computation time especially with the presence of an optimization algorithm as in this work.

3.3. MR dampers configuration

In this paper, MR dampers are configured inside each blade's aerofoil



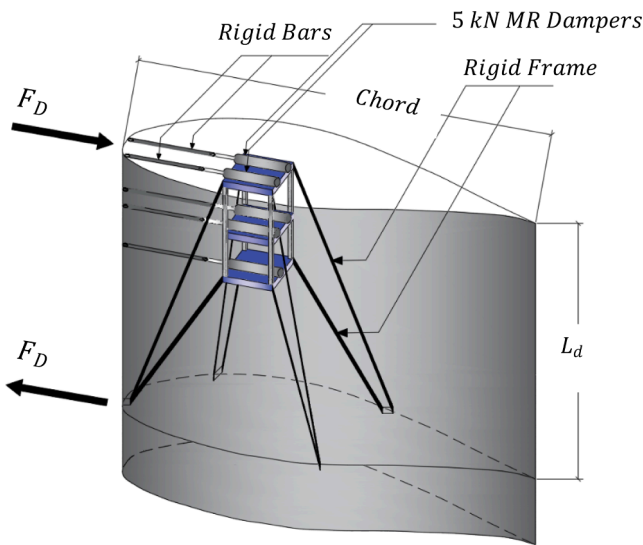


Fig. 8. MR dampers localization within an aerofoil illustration.

section at the blade tip as shown in Fig. 8. Moreover, each group of dampers is connected via a rigid frame between two plane sections, connected with the blade's inner walls, along a specific length L_d . MR dampers produce force when driven by the differential displacement and velocity between these two plane sections. It should be noted that a suitable design of the length L_d should be adopted so that the difference in displacements between the two planes does not exceed the given stroke of the damper and at the same time is enough to allow the excitation of dampers to produce an adequate control force. The number of actuation devices to be used inside each blade is also a crucial parameter however, several trials have been used in this work. It has been shown that the proposed MR dampers' configuration design has significantly succeeded in mitigating horizontal axis wind turbine vibrations in the edgewise direction. It is worth mentioning that the proposed actuator configuration is versatile in terms of accommodating the dampers inside the blade and at the tip. Furthermore, there is no need to have another structure (i.e., truss or frame) extending from the blade tip to the hub to mount actuators on as this will add extra weight to the system. Another advantage of the proposed system is that the proposed configuration does not hinder blade pitching about its axis and still the dampers operate at any pitch angle to suppress edgewise vibrations. Two different cases of configurations are adopted in this work as elaborated in section 5.3.

4. Optimized MR dampers proposed controller

4.1. LQR semi-active controller in MBC

As the mitigation of dynamic responses for turbine blades is crucial, a suitable controller should be designed to obtain the best possible reduction in responses while maintaining lowest power consumption. Optimal controllers based on LQR have been applied extensively in many structural control applications including onshore and offshore wind turbines and in civil engineering structures [3,6,9–11,43]. Optimal controllers tend to minimize structural responses while exerting minimum actuation forces. The latter is achieved by minimizing the quadratic cost function in Eq. (39) as

$$J = \frac{1}{2} \int_{t_i}^{t_f} \{X^T Q X + f_{cd}^T R f_{cd}\} dt \quad (39)$$

where Q and R are the cost function weighting matrices for system response and control force, respectively such that the former when

increased the controller decreases system responses on the cost of high control force. On the other hand, large values of R result in smaller damper forces with less reduction in dynamic responses.

As reported in [15], the designed regulator accounts only for the first mode shape of the blade. This is due to the fact that the majority of vibration is captured by the first mode only hence the feedback and state vector are going to be composed of three edgewise blades and side-to-side tower displacements in addition to their corresponding velocities. So, in total eight feedback DOF as

$$x(t) = \left\{ x_{1,im} x_{2,im} x_{3,im} x_{t,ss} \dot{x}_{1,im} \dot{x}_{2,im} \dot{x}_{3,im} \dot{x}_{t,ss} \right\}^T \quad (40)$$

As horizontal axis wind turbines are rotating, this results in time variant system properties. For optimal controller synthesis, which is based on LTI system matrices, transformation to non-rotating domain has been carried out in [15] through a Multi Blade Coordinate (MBC) transformation, also known as Coleman transformation. The state equation in MBC is expressed as

$$\dot{x}_{nr}(t) = A_{nr} x_{nr}(t) + B_{nr} (\Gamma_c F_d + Q_{ext,im}) \quad (41)$$

Such that A_{nr} and B_{nr} (where the subscript nr stand for non-rotating) are the plant and control matrices in the non-rotating frame, respectively and expressed as

$$A_{nr} = \begin{bmatrix} \mathbf{0}_{4 \times 4} & \mathbf{I}_{4 \times 4} \\ -M_{nr}^{-1} K_{nr} & -M_{nr}^{-1} C_{nr} \end{bmatrix}_{\in \mathbb{R}^{8 \times 8}} \quad (42)$$

and

$$B_{nr} = \begin{bmatrix} \mathbf{0}_{4 \times 3} \\ M_{nr}^{-1} D^{-1} \Gamma_e D_u \end{bmatrix}_{\in \mathbb{R}^{8 \times 3}}, \text{ where in-plane influence matrix} \quad (43)$$

$$\Gamma_e = \begin{bmatrix} 1 & 0 & 0 \\ 0 & 1 & 0 \\ 0 & 0 & 1 \\ 0 & 0 & 0 \end{bmatrix}$$

and the D matrix responsible for transformation of time-varying coordinates $\tilde{q}(t)$ to MBC $q_{nr}(t)$ non-rotating DOF is given as

$$D = \begin{bmatrix} 1 & \cos(\psi_1) & \sin(\psi_1) & 0 \\ 1 & \cos(\psi_2) & \sin(\psi_2) & 0 \\ 1 & \cos(\psi_3) & \sin(\psi_3) & 0 \\ 0 & 0 & 0 & 1 \end{bmatrix}_{\in \mathbb{R}^{4 \times 4}} \text{ and } D_u \quad (44)$$

$$= \begin{bmatrix} 1 & \cos(\psi_1) & \sin(\psi_1) \\ 1 & \cos(\psi_2) & \sin(\psi_2) \\ 1 & \cos(\psi_3) & \sin(\psi_3) \end{bmatrix}_{\in \mathbb{R}^{3 \times 3}}$$

The optimal control law can be formulated in the non-rotating frame as

$$u_{nr}(t) = -G_{nr} x_{nr}(t) \quad (45)$$

where G_{nr} is the feedback control gain computed as

$$G_{nr} = R_{nr}^{-1} B_{nr}^T P, R_{nr} = D_u^T R D_u \quad (46)$$

where P is the solution of the algebraic Ricatti equation given by

$$P A_{nr} + A_{nr}^T P - P B_{nr}^T R_{nr}^{-1} B_{nr} P + C_{nr}^T Q C_{nr} = 0, Q_{nr} = D_x^T Q D_x \quad (47)$$

MATALB, lqr function was used to solve for the algebraic Ricatti equation. Such that C_{nr} is the output matrix for output state equation and it should be an identity matrix for full state feedback purpose. The $x_{nr}(t)$ in Eq. (45) is the state vector expressed in the non-rotating frame and is transformed from $x(t)$ as

$$x_{nr}(t) = D_x^{-1} x(t), \text{ where } D_x = \begin{bmatrix} D & \mathbf{0}_{4 \times 4} \\ \hat{D} & D \end{bmatrix}_{\in \mathbb{R}^{8 \times 8}} \quad (48)$$

From Coleman transformation we have

$$\hat{D} = \Omega D_1, \quad D_1 = \begin{bmatrix} 0 & -\sin(\psi_1) & \cos(\psi_1) & 0 \\ 0 & -\sin(\psi_2) & \cos(\psi_2) & 0 \\ 0 & -\sin(\psi_3) & \cos(\psi_3) & 0 \\ 0 & 0 & 0 & 0 \end{bmatrix} \in \mathbb{R}^{4 \times 4} \quad (49)$$

Finally, the computed non-rotating frame control forces in Eq. (45) are transformed to time domain for application on the wind turbine numerical model via the MR dampers as

$$f_{cd}(t) = D_u u_{nr}(t) = \begin{Bmatrix} f_1 \\ f_2 \\ f_3 \end{Bmatrix} \quad (50)$$

4.2. Semi-active control optimization and damper voltage control

Assigning values for weighting matrices is usually done manually by trial-and-error which does not achieve fully optimal control [13,14,17,31,34]. In this work however, a PSO algorithm is used in conjunction with the LQR mentioned in section 4.1. to determine optimal values for weighting matrices to achieve the most possible reductions in blade's dynamic responses with minimum MR dampers forces exerted [32]. Moreover, the objective for using the PSO search algorithm is to minimize the average of the Mean Square Error (MSE) of the three blades' displacements. As for the MR dampers' voltage control, the FRBV method developed in [32] is adopted in this work since it is proven to over perform the conventional clipped voltage control.

5. Numerical example

5.1. Model description

In order to demonstrate the efficiency of the proposed optimized LQR semi-active PSO controller, numerical simulations using MATLAB were carried out. In this context, the benchmark 5-MW baseline horizontal axis wind turbine developed by Jonkman *et al.* is utilized for numerical simulation and testing [28]. However, the reduced model mentioned in section 4.1 is used for the controller synthesis. The numerical model developed for simulation accounts for the fundamental edgewise and flapwise modes for blades along with the fundamental side-to-side and fore-aft directions of the tower resulting in an 8-DOF system. Table 1 summarizes the specifications and dimensions for the used benchmark wind turbine. Note that all simulations are carried at the rated rotor speed $\Omega = 12.1 \text{ rpm}$. It should be noted that the pitch angle was selected equal to 0° since a pitch angle controller is not of scope of this paper and can be implemented in another study. In order to compute the appropriate shape functions (in-plane and out-of-plane) for the blade in hand needed for generalized solutions, BModes tool is used [44]. Edgewise and flapwise fundamental mode shapes are extracted as a function of the decremental span in a 6th order polynomial as depicted in Fig. 9 and expressed as

$$\begin{aligned} \phi_{in}(x) = & -0.6952 \left(\frac{x}{L_b}\right)^6 + 2.376 \left(\frac{x}{L_b}\right)^5 - 3.5772 \left(\frac{x}{L_b}\right)^4 + 2.5337 \left(\frac{x}{L_b}\right)^3 \\ & + 0.3627 \left(\frac{x}{L_b}\right)^2 \end{aligned} \quad (51)$$

$$\begin{aligned} \phi_{out}(x) = & -2.2555 \left(\frac{x}{L_b}\right)^6 + 4.7131 \left(\frac{x}{L_b}\right)^5 - 3.2452 \left(\frac{x}{L_b}\right)^4 + 1.7254 \left(\frac{x}{L_b}\right)^3 \\ & + 0.0622 \left(\frac{x}{L_b}\right)^2 \end{aligned}$$

5.2. Wind conditions

For testing to mimic real world application, appropriate modelling of

Table 1
5-MW benchmark wind turbine specifications.

General	
Max. Rated Power	5 MW
Rotor Orientation	Upwind
Number of Blades	3
Rotor Diameter	126 m
Hub Height	90 m
Cut-In, Rated, Cut-Out Wind Speeds	3 m/sec, 11.4 m/sec, 25 m/sec
Cut-In, Rated Rotor Speeds	6.9 rpm, 12.1 rpm
Rotor	
Hub Diameter	3 m
Hub Mass	56780 kg
Nacelle Mass	240,000 kg
Blade (LM 61.5 P2)	
Total Span	61.5 m
Overall Mass	17,740 kg
1st Edgewise Freq.	1.08 Hz
1st Flapwise Freq.	0.7 Hz
Structural Damping Ratio (all modes)	0.47 %
Tower	
Height above Ground	87.6 m
Overall Mass	347,460 kg
1st Side-to-Side Freq.	0.31 Hz
1st Fore-Aft Freq.	0.31 Hz
Structural Damping Ratio (all modes)	1.0 %

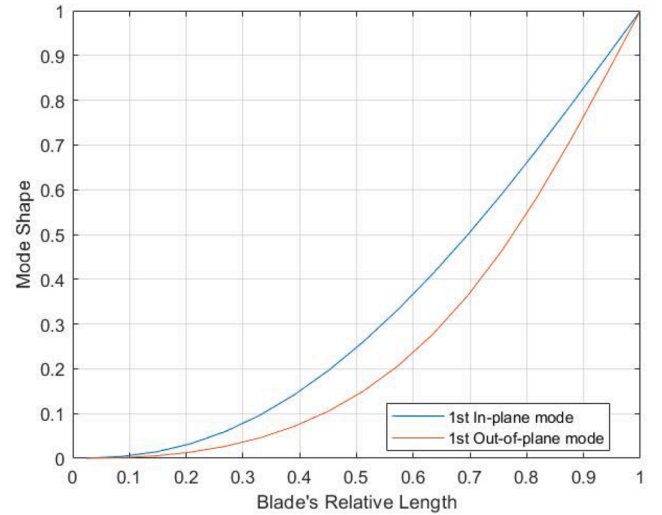


Fig. 9. Fundamental in-plane and out-of-plane blade modes shapes.

wind loads is crucial. In this context a steady mean wind speed at the hub height $\bar{V}_o = 12 \text{ m/sec}$ is assigned. As noted in Eq. (14), wind shear effects are considered as a cosine wave with $\Delta V_o = 2 \text{ m/sec}$. Moreover, a 1-D fully coherent turbulence following Kaimal spectrum is added to the harmonic wind speed resulting in a turbulent wind. Parameters for synthesizing the frequency spectrum in [45] are used. Time domain values were generated using IFFT of the produced frequency spectrum. Fig. 10 shows the overall turbulent wind at the tip implemented in simulations. It is worth mentioning that wind conditions were based on 10 min as recommended by the IEC 61400-1, however, 200 s were considered for plotting since it was found to be reliable representation for the investigated system to capture both the transient and steady state responses.

5.3. Controller design and Actuators' configuration

PSO was implemented to design a smart controller capable of controlling edgewise and flapwise blade displacements effectively. To verify the controller efficiency two MR dampers' locations and several

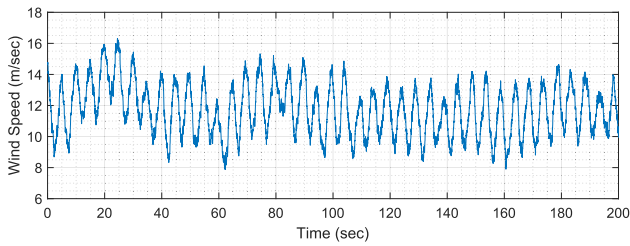


Fig. 10. Turbulent wind speed profile used.

numbers were implemented. Two cases namely Case A and Case B are defined.

In Case A, dampers are placed to control edgewise vibrations such that only one group of dampers is located at the blade tip (Fig. 11(a)). However, Case B accounts for employing two groups of MR dampers each consisting of five dampers as shown in Fig. 11(b). Five control modes were considered for Case A namely no dampers are installed, semi-active PSO, maximum voltage applied (passive on), half max. voltage applied and zero current applied (passive off) each having a different number of dampers: two, five, seven and nine dampers. For Case B, only semi-active control mode with five dampers in each group was tested to show the performance of the proposed PSO controller with adding additional MR dampers. Table 2 presents all the considered control scenarios.

For all Case A simulations, L_d is taken to be equal to 10m so that MR dampers are connected between the blade tip and at 51.5m from the hub. This 10m distance was determined through trial and error to optimize the MR damper force within the given damper stroke. It is worth mentioning that the 10m is explicit for the 5kN damper used. If designers should change the type of damper used, L_d may change accordingly to accommodate the stroke-suitable MR force relationship. However, L_d is doubled when considering Case B.

The PSO semi-active controller is optimized using the average of the MSE of tip displacements for the three blades as the fitness function value. For controller PSO-5A, as an example, swarm size is set to 6 particles, number of iterations is determined after the optimizer reaches the minimum goal value with maximum number of stall iterations 50 limited to 100. Fig. 12 shows the optimizer progress in reducing the cost

Table 2
All tested controllers.

MR dampers configuration	Mode	Tested Controller	
Case A	No control	Uncontrolled	
	Semi-active		PSO-2A
			PSO-5A
			PSO-7A
			PSO-9A
	Max. voltage passive on		PON-2A
			PON-5A
			PON-7A
	Half max. voltage passive on		PON-9A
			PON/2-2A
		PON/2-5A	
Passive off		PON/2-7A	
		PON/2-9A	
		POFF-2A	
		POFF-5A	
Case B	Semi-active	POFF-7A	
		POFF-9A	
		PSO-5A5B	

function.

5.4. Results and discussion

The 5-MW benchmark wind turbine was tested against configurations Case A and Case B. As noted in Figs. 13-16, blade tip displacement plots between the PSO semi-active controller, uncontrolled, and its corresponding passive control systems, that the proposed control algorithm has mitigated the dynamic response significantly. Time domain results are plotted for blade 1 as an example however, the other two blades witnessed a similar behaviour. Reductions in blade edgewise peak displacement exceeded 80% when using PSO-5A controller while only 73% using a passive controller with almost double the number of dampers (POFF-9A). As stated in Table 3, reductions in peak displacements using the semi-active PSO controller ranged from 62% with PSO-2A up to 81% with PSO-5A versus only from 26% using PON-2A and -5.00% using PON-9A (evident in Fig. 16(a)). As seen in Table 3 negative values for reductions in peak or peak-to-peak displacements means that responses were increased and that employing passive on control mode is not as effective as the proposed one. The latter is because

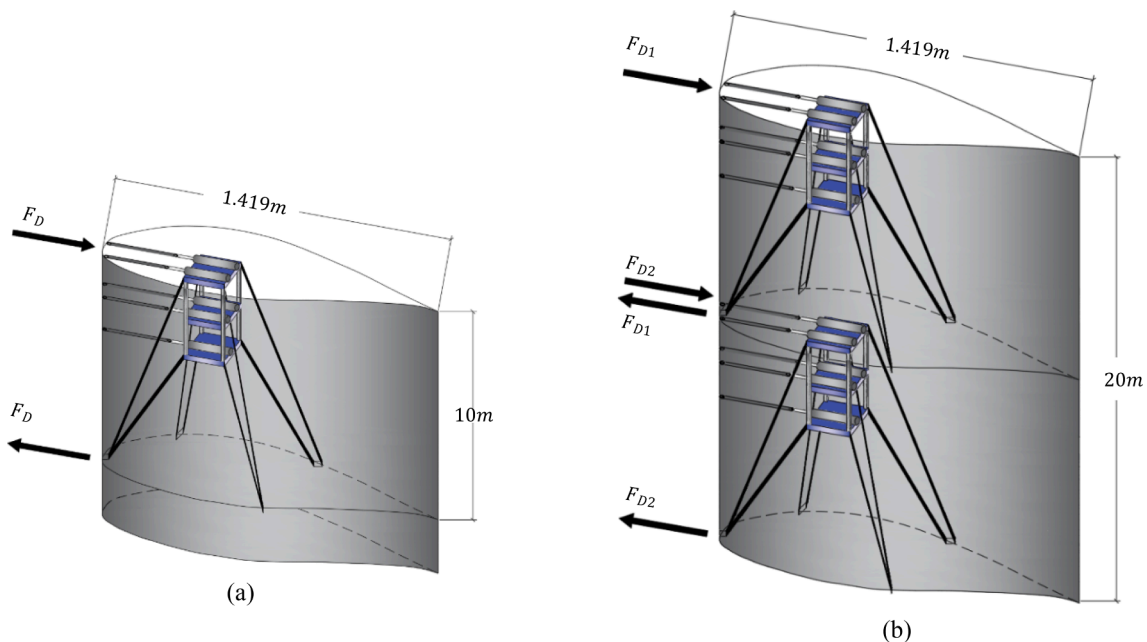


Fig. 11. Installation of five dampers within the blade's vicinity for (a) Case A (b) Case B.

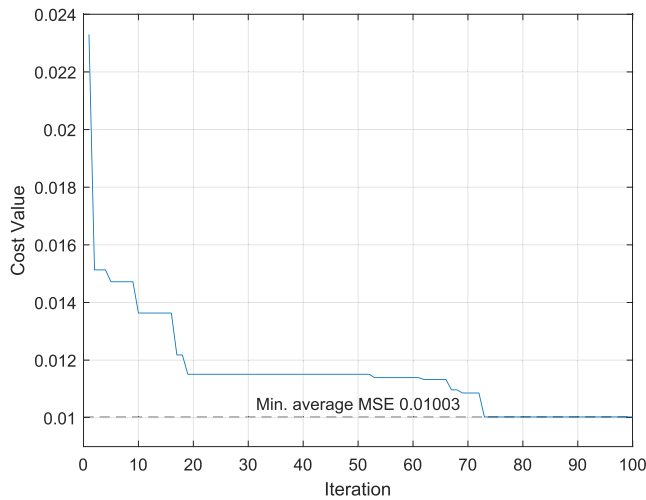


Fig. 12. Cost function history for PSO-5A controller optimization.

dampers can no longer provide flexibility and are acting as rigid elements thus, cannot act as energy sinks for excessive vibrations. On the other hand, better results were achieved using the half of max. voltage passive on and passive off control systems.

The same results were achieved also regarding reductions in the peak-to-peak displacement which is a crucial measure of the fatigue applied on the blade such that reductions ranged from 67% using PSO-2A up to 77% when using PSO-5A or PSO-7A. These results show that the proposed controller has a significant direct effect on promoting the longevity of blades and even better than passive on and off modes. All other results such as SD and RMS for the blade displacement are shown in Table 3 which prove the vast efficiency of the proposed system over the passive controllers.

The proposed algorithm makes full use of the actuator in hand thus the maximum force actuated in any case is the number of dampers employed multiplied by its force capacity (5kN). Although increasing the number of actuators helped in achieving more reduction in the peak displacement (increasing from two to five dampers), this is not a general trend.

As shown in Fig. 16(a), increasing the number of actuators to nine, within the same L_d , had the effect of increasing the displacement when

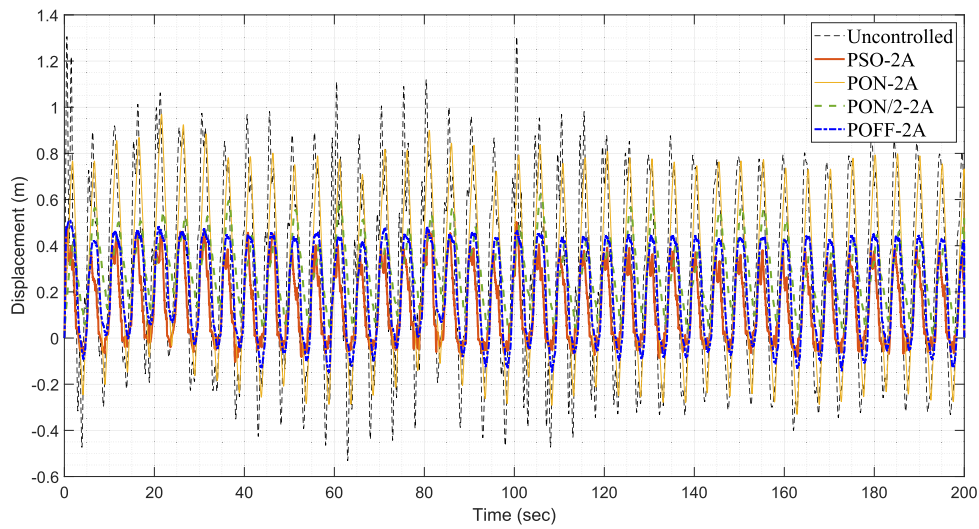


Fig. 13. Blade 1 displacement response for PSO-2A and passive controllers.

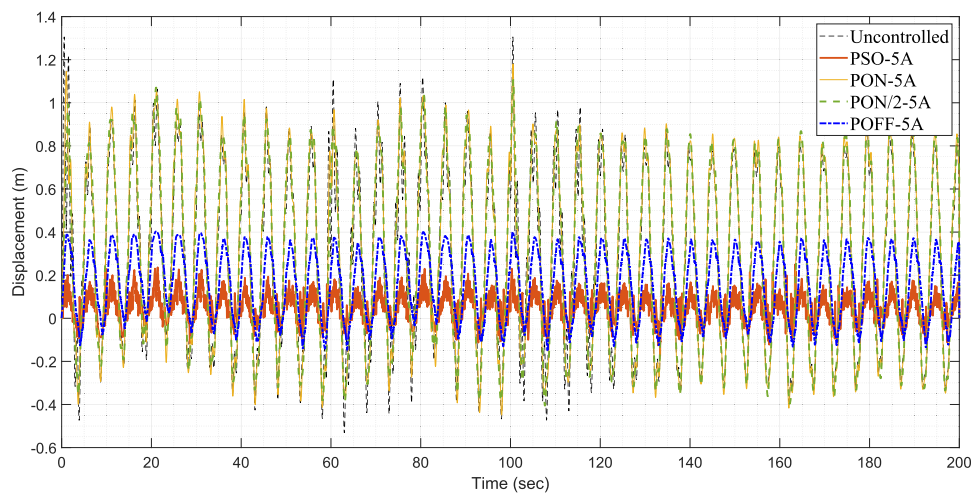


Fig. 14. Blade 1 displacement response for PSO-5A and passive controllers.

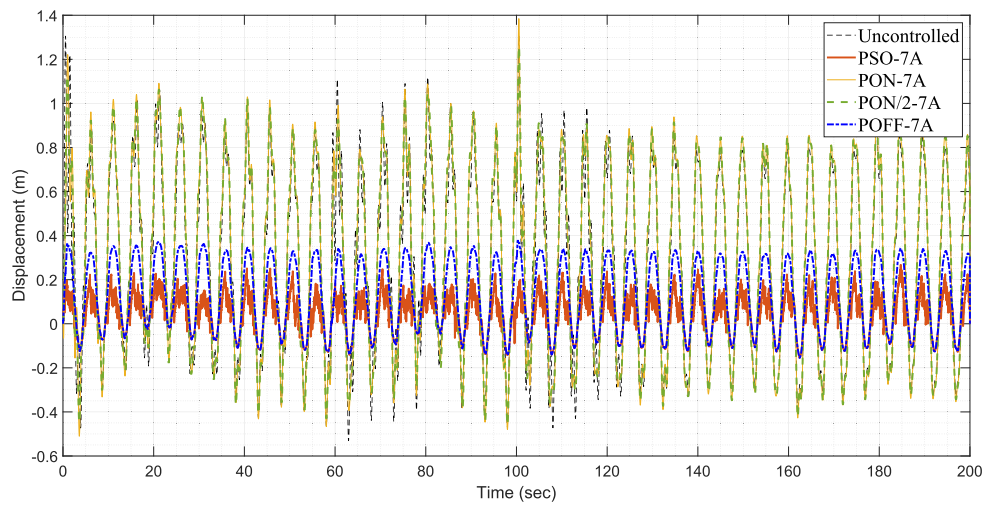


Fig. 15. Blade 1 displacement response for PSO-7A and passive controllers.

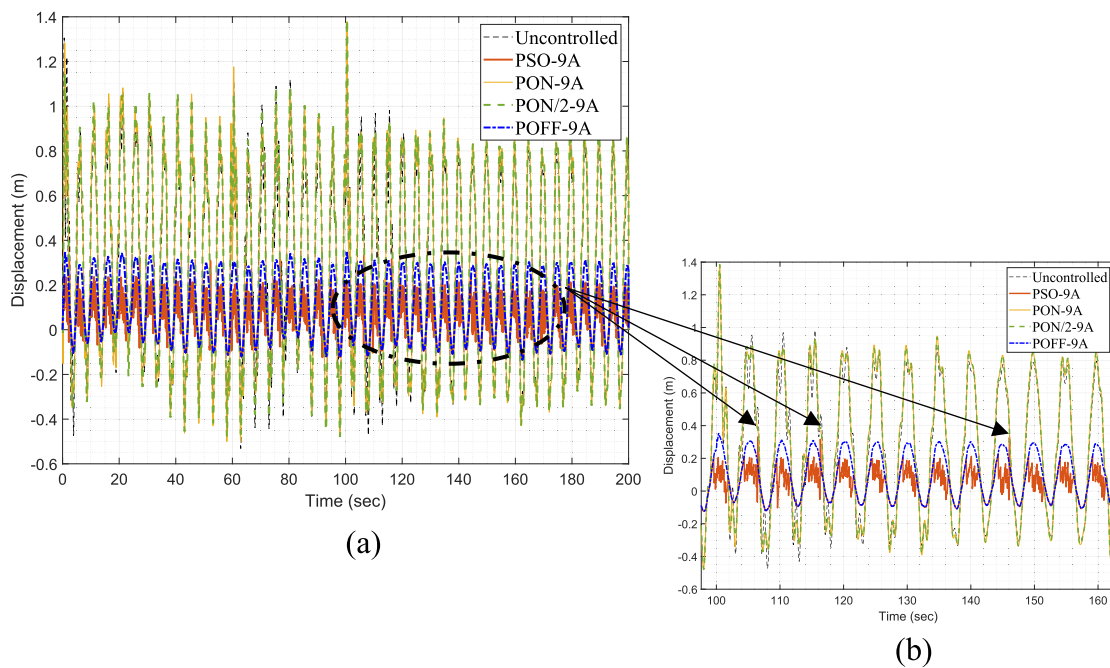


Fig. 16. (a) Blade 1 displacement response for PSO-9A and passive controllers. (b) Zoomed window showing spiked response.

this large number of dampers were actuated. The PSO controller optimized the actuators' behaviour to accommodate such a large number without overshooting. However, displacement spikes appeared in some instances (Fig. 16(b)). This latter behaviour explains why increasing the number of actuators is not necessarily the best option to displacement suppression as the controller will have to turn them to passive actuators to avoid overshooting.

Fig. 17(a) and 17(b) show bar charts for the percentage reductions in the peak and peak-to-peak displacements, respectively for the three blades applying all PSO controlled scenarios. As noted, the proposed controller shows robustness in reducing peak displacements and increasing blade's life span by reducing peak-to-peak displacements effectively. Moreover, it is seen that PSO-5A which constitutes five dampers always demonstrates the maximum reduction. Thus, it is recommended by authors to incorporate this case for controlling edgewise vibrations of wind turbine blades. As shown also in Fig. 17(a) and 17(b), bar chart diagrams illustrating how PSO-5A performed against its

passive counterparts. Notice that it has the highest percentage in reducing the peak and peak-to-peak displacements while consuming less energy. In conclusion, PSO-5A has been chosen the best controller. Another bar chart demonstration is shown in Fig. 18 where it demonstrates the performance of all the 5A controllers in the peak and peak-to-peak reductions. The PSO-5A controller again shows significant reductions of displacements in comparison to other control strategies employing the same number of dampers.

PSO-5A5B (Fig. 11(b)) is also tested to see the performance of the proposed controller versus different allocation of dampers. To choose the best controller between PSO-5A and PSO-5A5B, they were compared with each other. Fig. 19(a) shows the time domain displacement plots of PSO-5A and PSO-5A5B. Although PSO-5A5B is thought to decrease displacement further, because it uses double the number of actuators, it only slightly did. This is because the presence of the action and reaction forces produced along the same common plane where dampers are connected and thus, only a slight increase of force the additional five

Table 3
Simulation results achieved for Blade 1.

	Case	Peak Displacement (m)	Peak -to-Peak Displacement (m)	SD (m)	RMS Displacement (m)	Dampers Efficiency μ_d (%/kN)
Smart PSO Controller	Uncontrolled	1.31	1.84	0.40	0.49	
	PSO-2A	0.50 (62.0 %)	0.61 (67.0 %)	0.15 (61.0 %)	0.20	6.20
	PSO-5A	0.25 (81.0 %)	0.42 (77.0 %)	0.06 (83.6 %)	0.08	3.24
	PSO-7A	0.27 (79.0 %)	0.42 (77.0 %)	0.08 (77.9 %)	0.09	2.25
	PSO-9A	0.33 (75.0 %)	0.47 (74.0 %)	0.08 (78.3 %)	0.10	1.67
	PSO-5A5B	0.38 (71.0 %)	0.66 (64.0 %)	0.08 (78.0 %)	0.10	1.42
Passive On Control	PON-2A	0.97 (26.0 %)	1.30 (29.0 %)	0.33 (18.2 %)	0.43	
	PON-5A	1.18 (10.0 %)	1.63 (11.0 %)	0.41 (-3.90 %)	0.51	
	PON-7A	1.38 (-5.0 %)	1.90 (-3.00 %)	0.42 (-4.43 %)	0.51	
	PON-9A	1.38 (-5.0 %)	1.88 (-2.00 %)	0.42 (-5.02 %)	0.52	
Passive On (half max. voltage)	PON/2-2A	0.62 (53.0 %)	0.62 (66.0 %)	0.14 (64.0 %)	0.31	
	PON/2-5A	1.11 (15.0 %)	1.51 (18.0 %)	0.41 (-2.90 %)	0.51	
	PON/2-7A	1.26 (4.00 %)	1.71 (7.00 %)	0.42 (-3.97 %)	0.51	
	PON/2-9A	1.39 (-6.00 %)	1.86 (-1.00 %)	0.42 (-4.70 %)	0.52	
Passive off Control	POFF-2A	0.51 (61.0 %)	0.66 (64.0 %)	0.19 (51.3 %)	0.28	
	POFF-5A	0.40 (69.0 %)	0.56 (70.0 %)	0.15 (60.5 %)	0.22	
	POFF-7A	0.38 (71.0 %)	0.53 (71.0 %)	0.16 (60.2 %)	0.20	
	POFF-9A	0.35 (73.0 %)	0.49 (73.0 %)	0.14 (64.7 %)	0.18	

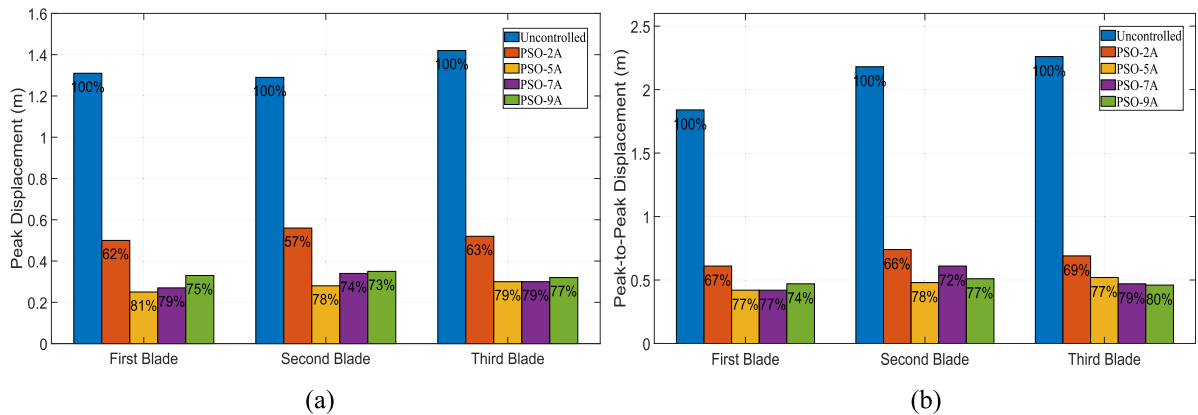


Fig. 17. Bar chart for percentage reductions for all PSO controllers in (a) peak displacement response. (b) peak-to-peak response.

dampers added. Furthermore, spiked displacement continues to be witnessed for this case as well as PSO-7A and PSO-9A (Fig. 19(b)) due to the use of high numbers of actuators which shows that PSO-5A is again better than PSO-5A5B with only half the number of actuators.

To measure how effective dampers are operating through the proposed control strategy, an efficiency term is introduced, μ_d . This term measures how much percentage reduction in peak response can a 1kN force achieve. Fig. 20 shows the performance of Case A configurations. It is concluded again that controller PSO-5A is the best in terms of achieving the highest percentage of reduction in peak response whilst the best also in efficiency. Though PSO-2A has higher efficiency, it cannot be chosen as it does not suppress displacements as effectively. It

is worth mentioning that the maximum exerted force in PSO-5A was only 2.5ton which is only 14% of the total blade weight. In addition, this value is equal to only half of that achieved by [15] with much higher peak displacement reduction.

6. Conclusion and future work

In this work, a novel approach of utilizing MR dampers to enhance wind turbine performance has been proposed and implemented. More specifically, a PSO semi-active controller has been designed to mitigate undesirable edgewise blade dynamic responses. Actuators have been modelled using NNs to increase robustness and prevent response lag

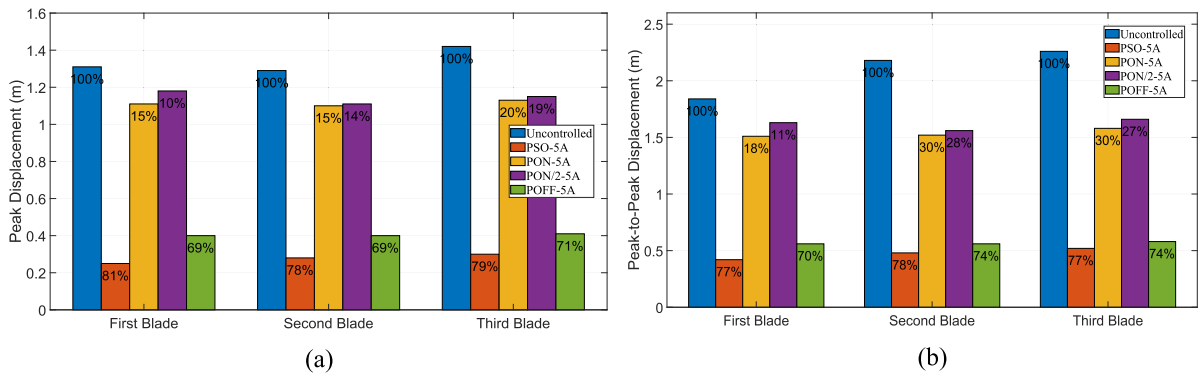


Fig. 18. Bar chart for percentage reductions for PSO-5A in (a) peak displacement response. (b) peak-to-peak response.

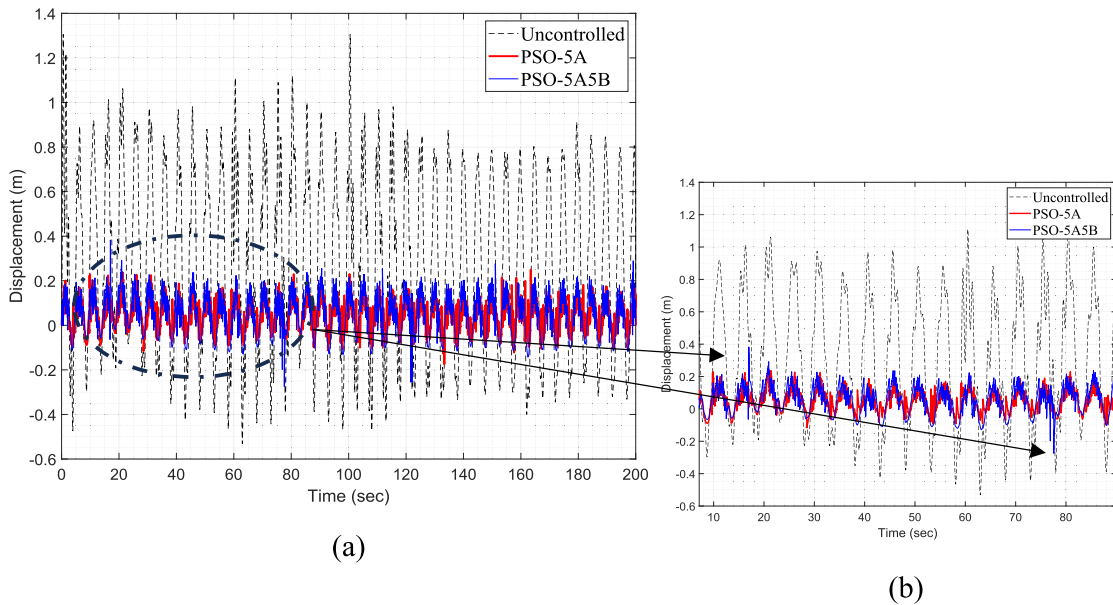


Fig. 19. Blade 1 displacement response for (a) PSO-5A and PSO-5A5B controllers. (b) Zoomed window showing spiked responses.

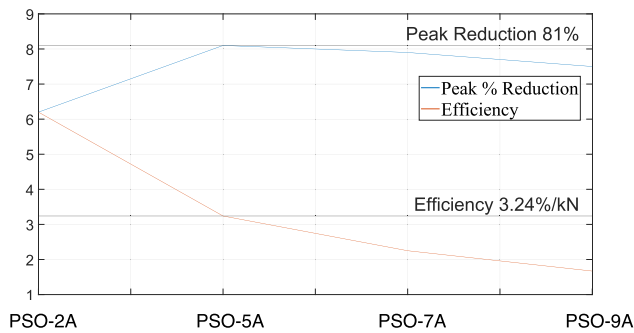


Fig. 20. Relationship between PSO controllers in peak reduction and efficiency.

encountered with conventional methods. A 5-MW benchmark wind turbine has been used for testing and simulation of the proposed controller and comparison against passive ON/OFF controllers. Two different scenarios for control devices configuration have been proposed. Case A configuration entails that only one group of MR dampers be placed at the blade tip.

On the other hand, Case B configuration consists of two groups of

dampers placed along the blade’s span. The proposed configuration is practical as it does not require a super mounting structure extending along the whole span of the wind turbine blade which might exceed 80m in some cases. Though clipped voltage control is common among MR voltage controllers, FRBV method is implemented in this work which delivers a more flexible control concept.

Significant results have been obtained exceeding a reduction of 80% in the peak displacement response of the blade. A comparative assessment of four different controllers for Case A have also been carried out among which, PSO-5A have proven to have the best performance in reducing edgewise vibration and thus is recommended by the authors.

In addition to peak performance, the proposed controller promotes longevity of wind turbine blades as it has a superior effect on reducing peak-to-peak responses by mitigating over 77% of the uncontrolled response. Efforts are currently being put into further research on optimizing the placement for MR dampers within the blade’s vicinity. Moreover, work considers stabilizing disturbances that happen in the generated power due to structural dynamic motions.

CRedit authorship contribution statement

Duan Fang: Methodology, Resources, Visualization. **Mohammad Osman Tokhi:** Conceptualization, Project administration, Supervision, Writing – review & editing. **Shady Salem:** Conceptualization, Project

administration, Supervision, Writing – review & editing.

the work reported in this paper.

Declaration of Competing Interest

The authors declare that they have no known competing financial interests or personal relationships that could have appeared to influence

Data availability

Data will be made available on request.

Appendix A. . Horizontal axis wind turbine time variant system matrices

Mass Matrix

$$M(t) = \begin{bmatrix} M_2 & 0 & 0 & M_{1,1} \\ 0 & M_2 & 0 & M_{1,2} \\ 0 & 0 & M_2 & M_{1,3} \\ M_{1,1}^T & M_{1,2}^T & M_{1,3}^T & M_T \end{bmatrix}_{\in R^{8 \times 8}} \tag{A.1}$$

Where,

$$M_2 = \begin{bmatrix} m_{2,in} & 0 \\ 0 & m_{2,out} \end{bmatrix}_{\in R^{2 \times 2}} \quad M_{1,j}(t) = \begin{bmatrix} m_{1,in,j}(t) & 0 \\ 0 & m_{1,out} \end{bmatrix}_{\in R^{2 \times 2}} \tag{A.2}$$

$$M_T = \begin{bmatrix} m_{T,ss} & 0 \\ 0 & m_{T,fa} \end{bmatrix}_{\in R^{2 \times 2}}$$

such that

$$m_{1,in,j}(t) = \int_0^{L_b} \mu_b(x) \phi_{in}(x) dx \cos(\psi_j) \quad \text{and} \quad m_{1,out} = \int_0^{L_b} \mu_b(x) \phi_{out}(x) dx \tag{A.3}$$

$$m_{2,i} = \int_0^{L_b} \mu_b(x) \phi_{in}^2(x) dx$$

$$m_{T,h} = 3 \int_0^{L_b} \mu_b(x) dx + M_{nac} + \int_0^{L_T} \mu_T(x) \phi_h^2(z) dz$$

Stiffness Matrix

$$K(t) = \bar{K}(t, \Omega) + K_{\Omega}(t, \dot{\Omega}) \tag{A.4}$$

Where

$$\bar{K}(t, \Omega) = \begin{bmatrix} K_1 + K_{g,1} & 0 & 0 & 0 \\ 0 & K_1 + K_{g,2} & 0 & 0 \\ 0 & 0 & K_1 + K_{g,3} & 0 \\ -\Omega^2 \bar{M}_{4,1}^T & -\Omega^2 \bar{M}_{4,2}^T & -\Omega^2 \bar{M}_{4,3}^T & K_T \end{bmatrix}_{\in R^{8 \times 8}} \tag{A.5}$$

and

$$K_1 = \begin{bmatrix} k_{e,inin} + \Omega^2(k_{e,in} - m_{2,in}) & 0 \\ 0 & k_{e,outout} + \Omega^2(k_{e,out} - m_{2,out}) \end{bmatrix}_{\in R^{2 \times 2}} \tag{A.6}$$

$$K_{g,j} = \begin{bmatrix} k_{g,j,in} \cos(\psi_j) & 0 \\ 0 & k_{g,j,out} \cos(\psi_j) \end{bmatrix}_{\in R^{2 \times 2}}$$

$$\bar{M}_{4,j}(t) = \begin{bmatrix} m_{1,in,j}(t) \sin(\psi_j) & 0 \\ 0 & 0 \end{bmatrix}_{\in R^{2 \times 2}}$$

$$K_T = \begin{bmatrix} \int_0^{L_T} EI(z) (\phi_{ss}''(z))^2 dz & 0 \\ 0 & \int_0^{L_T} EI(z) (\phi_{fa}''(z))^2 dz \end{bmatrix}_{\in R^{2 \times 2}}$$

$$K_1 = \begin{bmatrix} k_{e,inin} + \Omega^2(k_{e,in} - m_{2,in}) & 0 \\ 0 & k_{e,outout} + \Omega^2(k_{e,out} - m_{2,out}) \end{bmatrix}_{\in R^{2 \times 2}} \tag{A.7}$$

$$K_{g,j} = \begin{bmatrix} k_{g,j,in} \cos(\psi_j) & 0 \\ 0 & k_{g,j,out} \cos(\psi_j) \end{bmatrix}_{\in R^{2 \times 2}}$$

$$\bar{M}_{4,j}(t) = \begin{bmatrix} m_{1,in,j}(t) \sin(\psi_j) & 0 \\ 0 & 0 \end{bmatrix}_{\in R^{2 \times 2}}$$

$$K_T = \begin{bmatrix} \int_0^{L_T} EI(z)(\phi_{ss}''(z))^2 dz & 0 \\ 0 & \int_0^{L_T} EI(z)(\phi_{fa}''(z))^2 dz \end{bmatrix}_{\in R^{2 \times 2}}$$

and

$$\bar{K}(t, \Omega) = \begin{bmatrix} 0 & 0 & 0 & 0 \\ 0 & 0 & 0 & 0 \\ 0 & 0 & 0 & 0 \\ -\dot{\Omega}(t)\bar{M}_{4,1}^T & -\dot{\Omega}(t)\bar{M}_{4,2}^T & -\dot{\Omega}(t)\bar{M}_{4,3}^T & 0 \end{bmatrix}_{\in R^{8 \times 8}} \tag{A.8}$$

Damping Matrix

$$C(t) = C_s(t) + C_a + \bar{C}(t) \tag{A.9}$$

where

$$C_s(t) = \begin{bmatrix} C_{sb} & 0 & 0 & 0 \\ 0 & C_{sb} & 0 & 0 \\ 0 & 0 & C_{sb} & 0 \\ 0 & 0 & 0 & C_{sT} \end{bmatrix}_{\in R^{8 \times 8}} \tag{A.10}$$

$$C_{sb}(t) = \begin{bmatrix} \alpha_{cb,in}m_{2,in} + \beta_{cb,in}k_{e,in} & 0 \\ 0 & \alpha_{cb,out}m_{2,out} + \beta_{cb,out}k_{e,out} \end{bmatrix}_{\in R^{2 \times 2}}$$

$$C_{sT}(t) = \begin{bmatrix} \alpha_{cT,ss}m_{T,ss} + \beta_{cT,ss}K_T[1, 1] & 0 \\ 0 & \alpha_{cT,fa}m_{T,fa} + \beta_{cT,fa}K_T[2, 2] \end{bmatrix}_{\in R^{2 \times 2}}$$

and

$$C_a = \begin{bmatrix} C_{ab} & 0 & 0 & 0 \\ 0 & C_{ab} & 0 & 0 \\ 0 & 0 & C_{ab} & 0 \\ 0 & 0 & 0 & C_{aT} \end{bmatrix}_{\in R^{8 \times 8}} \tag{A.11}$$

$$\bar{C}(t) = \begin{bmatrix} 0 & 0 & 0 & 0 \\ 0 & 0 & 0 & 0 \\ 0 & 0 & 0 & 0 \\ -2\Omega(t)\bar{M}_{4,1}^T & -2\Omega(t)\bar{M}_{4,2}^T & -2\Omega(t)\bar{M}_{4,3}^T & 0 \end{bmatrix}_{\in R^{8 \times 8}} \tag{A.12}$$

References

[1] Letcher TM. Wind energy engineering: A handbook for onshore and offshore wind turbines. Academic Press; 2017.

[2] IEA. Wind Electricity, IEA, Paris 2022. <https://www.iea.org/reports/wind-electricity> (accessed January 30, 2023).

[3] Zuo H, Bi K, Hao H. A state-of-the-art review on the vibration mitigation of wind turbines. Renew. Sustain. Energy Rev. 2020;121:109710. <https://doi.org/10.1016/j.rser.2020.109710>.

[4] GE's Most Powerful Onshore Wind Turbine Gets Even More Powerful n.d. <https://www.ge.com/news/press-releases/ge-most-powerful-onshore-wind-turbine-gets-even-more-powerful> (accessed February 12, 2023).

[5] Karimirad M. Offshore energy structures for wind power, wave energy and hybrid marine platforms. Springer; 2014.

[6] Spencer Jr BF, Nagarajaiah S. State of the Art of Structural Control. J. Struct. Eng. 2003;129:845–56. [https://doi.org/10.1061/\(ASCE\)0733-9445\(2003\)129:7\(845\)](https://doi.org/10.1061/(ASCE)0733-9445(2003)129:7(845)).

[7] Ou JP, Li H. The state-of-the-art and practice of structural control of civil structures for hazard mitigation in mainland china. ItkAcln 2008.

[8] Kumar EV, Jerome J. An adaptive particle swarm optimization algorithm for robust trajectory tracking of a class of under actuated system. Arch. Elect. Eng. 2014;63: 345–65. <https://doi.org/10.2478/ae-2014-0026>.

[9] Saaed TE, Nikolakopoulos G, Jonasson JE, Hedlund H. A state-of-the-art review of structural control systems. JVC/Journal of Vibration and Control 2015;21:919–37. <https://doi.org/10.1177/1077546313478294>.

[10] Njiri JG, Söffker D. State-of-the-art in wind turbine control: Trends and challenges. Renew. Sustain. Energy Rev. 2016;60:377–93. <https://doi.org/10.1016/j.rser.2016.01.110>.

[11] Yang Y, Musa B, Yue M-N, Li C. A review on the state-of-the-art of seismic analysis of wind turbines reneng dongli gongcheng. Journal of Engineering for Thermal Energy and Power 2019;34. <https://doi.org/10.16146/j.cnki.mdjgc.2019.09.002>.

[12] Xie F, Aly AM. Structural control and vibration issues in wind turbines: A review. Eng. Struct. 2020;210:110087. <https://doi.org/10.1016/j.engstruct.2019.110087>.

[13] Fitzgerald B, Basu B, Nielsen SRK. Active tuned mass dampers for control of in-plane vibrations of wind turbine blades. Struct. Control Health Monit. 2013;20: 1377–96. <https://doi.org/10.1002/stc.1524>.

[14] Staino A, Basu B. Dynamics and control of vibrations in wind turbines with variable rotor speed. Eng. Struct. 2013;56:58–67. <https://doi.org/10.1016/j.engstruct.2013.03.014>.

[15] Staino A, Basu B, Nielsen SRK. Actuator control of edgewise vibrations in wind turbine blades. J. Sound Vib. 2012;331:1233–56. <https://doi.org/10.1016/j.jsv.2011.11.003>.

[16] Zhang Z, Staino A, Basu B, Nielsen SRK. Performance evaluation of full-scale tuned liquid dampers (TLDs) for vibration control of large wind turbines using real-time hybrid testing. Eng. Struct. 2016;126:417–31. <https://doi.org/10.1016/j.engstruct.2016.07.008>.

[17] Sarkar S, Chakraborty A. Optimal design of semiactive MR-TLCD for along-wind vibration control of horizontal axis wind turbine tower. Struct. Control Health Monit. 2018;25:1–18. <https://doi.org/10.1002/stc.2083>.

[18] Caterino N. Semi-active control of a wind turbine via magnetorheological dampers. J. Sound Vib. 2015;345:1–17. <https://doi.org/10.1016/j.jsv.2015.01.022>.

[19] Chen J, Yuan C, Li J, Xu Q. Semi-active fuzzy control of edgewise vibrations in wind turbine blades under extreme wind. Journal of Wind Engineering and Industrial Aerodynamics 2015;147:251–61. <https://doi.org/10.1016/j.jweia.2015.10.012>.

[20] Kumar G, Kumar A, Jakka RS. An adaptive LQR controller based on PSO and maximum predominant frequency approach for semi-active control scheme using MR damper. Mechanics & Industry 2018;19:109. <https://doi.org/10.1051/meca/2018018>.

[21] Wang DH, Liao WH. Modeling and control of magnetorheological fluid dampers using neural networks. Smart Mater. Struct. 2005;14:111–26. <https://doi.org/10.1088/0964-1726/14/1/011>.

[22] Chopra AK. Dynamics of structures : theory and applications to earthquake engineering, 4/E. 2012.

[23] Hansen MH. Improved modal dynamics of wind turbines to avoid stall-induced vibrations. Wind Energy 2003;6:179–95. <https://doi.org/10.1002/we.79>.

[24] Burton T, Jenkins N, Sharpe D, Bossanyi E. Wind Energy Handbook. Second Edi. John Wiley & Sons, Ltd; 2011.

[25] DJ Cerda S, Van der Temple J. AERODYNAMIC DAMPING IN THE DESIGN OF SUPPORT STURCTURES FOR OFFSHORE WIND TURBINES. Paper of the Copenhagen offshore conference, 2005, p. 1–9.

- [26] R. D. S. Bentley RJ. Dynamics of structures by Ray W. Clough and Joseph Penzien. Third Edit. McGraw-Hill; 1977. <https://doi.org/10.1201/b11772>.
- [27] Y. Cheng F, Jiang H, Lou K. Smart Structures Innovative Systems for Seismic Response Control. CRC press: Taylor and Francis Group; 2008.
- [28] Jonkman J, Butterfield S, Musial W, Scott G. Definition of a 5-MW reference wind turbine for offshore system development. 2009.
- [29] Hansen M. Aerodynamics of Wind Turbines. Routledge Taylor & Francis Group; 2015. <https://doi.org/10.1049/ip-a-1.1983.0080>.
- [30] Jung H-J, Spencer BF, Lee I-W. Control of seismically excited cable-stayed bridge employing magnetorheological fluid dampers. J. Struct. Eng. 2003;129:873–83. [https://doi.org/10.1061/\(ASCE\)0733-9445\(2003\)129:7\(873\)](https://doi.org/10.1061/(ASCE)0733-9445(2003)129:7(873)).
- [31] Yoshida, Osamu and SJD. Response control of full-scale irregular buildings using magnetorheological dampers. Journal of Structural Engineering 2005;131:734–42. [https://doi.org/10.1061/\(ASCE\)0733-9445\(2005\)131:5\(734\)](https://doi.org/10.1061/(ASCE)0733-9445(2005)131:5(734)).
- [32] Fakhry P, Torky AA, Rashed YF. Optimized seismic response control of coupled fem-bem high-rise structural models using magnetorheological dampers. J. Earthq. Eng. 2021;26:1–28. <https://doi.org/10.1080/13632469.2021.1987355>.
- [33] Braz-César M, Barros R. Optimal control of a plan asymmetric structure using magnetorheological dampers. Arch. Appl. Mech. 2017;87:893–904. <https://doi.org/10.1007/s00419-016-1191-z>.
- [34] Ohtori Y, Christenson RE, Spencer BF, Dyke SJ. Benchmark control problems for seismically excited nonlinear buildings. J. Eng. Mech. 2004;130:366–85. [https://doi.org/10.1061/\(ASCE\)0733-9399\(2004\)130:4\(366\)](https://doi.org/10.1061/(ASCE)0733-9399(2004)130:4(366)).
- [35] Jothinathan S, Kashyap S, Kumar D, Saha N. Response control of fixed offshore structure with wind turbine using MR damper. In: Oceans Conference Record (IEEE), Institute of Electrical and Electronics Engineers Inc; 2022. <https://doi.org/10.1109/OCEANSChennai45887.2022.9775436>.
- [36] Martynowicz P. Control of a magnetorheological tuned vibration absorber for wind turbine application utilising the refined force tracking algorithm. Journal of Low Frequency Noise Vibration and Active Control 2017;36:339–53. <https://doi.org/10.1177/1461348417744299>.
- [37] Sun C. Semi-active control of monopile offshore wind turbines under multi-hazards. Mech. Syst. Sig. Process. 2018;99:285–305. <https://doi.org/10.1016/j.ymssp.2017.06.016>.
- [38] Spencer BF, Jr, Dyke SJ, Sain MK, Carlson JD. Phenomenological model for magnetorheological dampers. J. Eng. Mech. 1997;123:230–8. [https://doi.org/10.1061/\(ASCE\)0733-9399\(1997\)123:3\(230\)](https://doi.org/10.1061/(ASCE)0733-9399(1997)123:3(230)).
- [39] Dyke SJ, Spencer BF, Sain MK, Carlson JD. Modeling and control of magnetorheological dampers for seismic response reduction. Smart Mater. Struct. 1996;5:565–75. <https://doi.org/10.1088/0964-1726/5/5/006>.
- [40] Xu ZD, Shen YP, Guo YQ. Semi-active control of structures incorporated with magnetorheological dampers using neural networks. Smart Mater. Struct. 2003;12:80–7. <https://doi.org/10.1088/0964-1726/12/1/309>.
- [41] Wei S, Wang J, Ou J. Method for improving the neural network model of the magnetorheological damper. Mech. Syst. Sig. Process. 2021;149:107316. <https://doi.org/10.1016/j.ymssp.2020.107316>.
- [42] Şahin Ö, Gökhan Adar N, Kemerli M, Çağlar N, Şahin İ, Parlak Z, et al. A comparative evaluation of semi-active control algorithms for real-time seismic protection of buildings via magnetorheological fluid dampers. Journal of Building Engineering 2021;42. <https://doi.org/10.1016/j.jobte.2021.102795>.
- [43] Fakhry P, Salem S, O.Tokhi M, Fang D. Robust structural control of onshore wind turbines using MR dampers. 2023 Prognostics and Health Management Conference (PHM), Paris, France: IEEE; 2023, p. 300–6. <https://doi.org/10.1109/PHM58589.2023.00062>.
- [44] Bir GS. User's Guide to BModes. National Renewable Energy Laboratory; 2007.
- [45] Murtagh PJ, Basu B, Broderick BM. Along-wind response of a wind turbine tower with blade coupling subjected to rotationally sampled wind loading 2005;27: 1209–19. <https://doi.org/10.1016/j.engstruct.2005.03.004>.